

# PGC-1 $\alpha$ mediates mitochondrial biogenesis and oxidative phosphorylation in cancer cells to promote metastasis

Valerie S. LeBleu<sup>1,2</sup>, Joyce T. O'Connell<sup>2</sup>, Karina N. Gonzalez Herrera<sup>3</sup>, Harriet Wikman<sup>4</sup>, Klaus Pantel<sup>4</sup>, Marcia C. Haigis<sup>3</sup>, Fernanda Machado de Carvalho<sup>5</sup>, Aline Damascena<sup>5</sup>, Ludmilla Thome Domingos Chinen<sup>5</sup>, Rafael M. Rocha<sup>5</sup>, John M. Asara<sup>6,7</sup> and Raghu Kalluri<sup>1,2,8</sup>

**Cancer cells can divert metabolites into anabolic pathways to support their rapid proliferation and to accumulate the cellular building blocks required for tumour growth. However, the specific bioenergetic profile of invasive and metastatic cancer cells is unknown. Here we report that migratory/invasive cancer cells specifically favour mitochondrial respiration and increased ATP production. Invasive cancer cells use the transcription coactivator peroxisome proliferator-activated receptor gamma, coactivator 1 alpha (PPARGC1A, also known as PGC-1 $\alpha$ ) to enhance oxidative phosphorylation, mitochondrial biogenesis and the oxygen consumption rate. Clinical analysis of human invasive breast cancers revealed a strong correlation between PGC-1 $\alpha$  expression in invasive cancer cells and the formation of distant metastases. Silencing of PGC-1 $\alpha$  in cancer cells suspended their invasive potential and attenuated metastasis without affecting proliferation, primary tumour growth or the epithelial-to-mesenchymal program. Inherent genetics of cancer cells can determine the transcriptome framework associated with invasion and metastasis, and mitochondrial biogenesis and respiration induced by PGC-1 $\alpha$  are also essential for functional motility of cancer cells and metastasis.**

It is generally well established that dividing cells, including cancer cells, meet their metabolic demands through the process of aerobic glycolysis<sup>1,2</sup>. The energy generated through aerobic glycolysis is thought to be sufficient to offset the energy demands associated with rapid cancer cell division, while simultaneously allowing accumulation of biosynthetic precursors needed for anabolic reactions<sup>1,2</sup>. Despite enhanced glycolysis, cancer cells also operate mitochondrial respiration to derive a significant fraction of their ATP (ref. 3). In a growing tumour, adaptive metabolic reprogramming, precipitated in part by oncogenic transformation<sup>4</sup>, gives cancer cells a proliferative advantage<sup>5,6</sup>. The autonomous metabolic reprogramming of rapidly proliferating cancer cells promotes self-sustaining signal transduction mechanisms to foster growth and survival<sup>5</sup>. However, the metabolic requirements of invasive and metastatic cancer cells that suspend their proliferative program to acquire a migratory phenotype are unknown. An improved understanding of the energetic demands of invading cancer cells may

inform therapeutic strategies to impair metastasis, the primary reason for death in cancer patients. We set out to conduct experiments to study the specific energy requirements of invasive and metastatic cancer cells, with a hope of unraveling additional mechanisms of metastasis.

## RESULTS

### Circulating cancer cells exhibit enhanced mitochondria biogenesis and respiration

GFP-labelled 4T1 mammary epithelial cancer cells were orthotopically implanted in the mammary fat pads of mice (Fig. 1a,b). Primary tumours emerge following implantation of cancer cells into the mammary fat pads of female mice and lung metastases develop with 100% penetrance<sup>7</sup>. Circulating cancer cells (CCCs, also referred to as circulating tumour cells or CTCs) and cancer cells from the primary tumours (PCCs) and metastatic lungs (MCCs) were purified by fluorescence-activated cell sorting (FACS) and their transcriptomes

<sup>1</sup>Department of Cancer Biology, Metastasis Research Center, University of Texas MD Anderson Cancer Center, Houston, Texas 77054, USA. <sup>2</sup>Division of Matrix Biology, Department of Medicine, Beth Israel Deaconess Medical Center, Boston, Massachusetts 02115, USA. <sup>3</sup>Department of Cell Biology, Paul F. Glenn Laboratories for the Biological Mechanisms of Aging, Harvard Medical School, Boston, Massachusetts 02115, USA. <sup>4</sup>Department of Tumor Biology, University Medical Center Hamburg-Eppendorf, Martinistrasse 52, D-20246 Hamburg, Germany. <sup>5</sup>International Research Center, A. C. Camargo Cancer Center, 01509-010, Sao Paulo, Brazil. <sup>6</sup>Division of Signal Transduction, Beth Israel Deaconess Medical Center, Boston, Massachusetts 02115, USA. <sup>7</sup>Department of Medicine, Harvard Medical School, Boston, Massachusetts 02115, USA.

<sup>8</sup>Correspondence should be addressed to R.K. (e-mail: rkalluri@mdanderson.org)

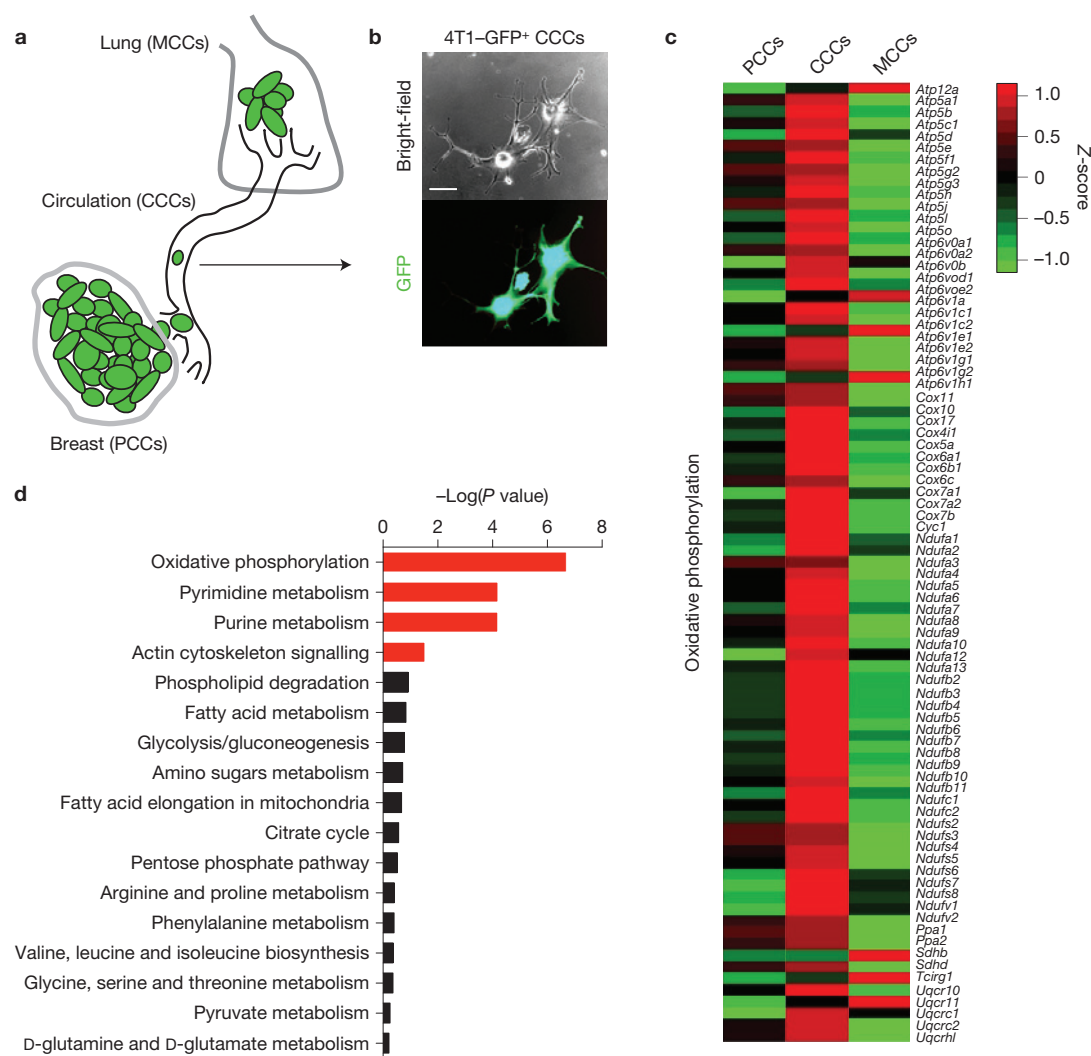


**Figure 1** CCCs exhibit enhanced oxidative phosphorylation. **(a)** 4T1-GFP<sup>+</sup> cells were injected orthotopically into the mammary fat pad of mice and PCCs, CCCs and MCCs were purified by FACS sorting for gene expression profiling assays. **(b)** Representative image of CCCs isolated from the 4T1 orthotopic tumour model based on their GFP expression. Scale bar, 10  $\mu$ m. **(c)** Heat map of differentially regulated genes in the oxidative phosphorylation

gene set in PCCs, CCCs and MCCs. **(d)** Pathway analyses of transcriptomes of CCCs compared with PCCs identify oxidative phosphorylation as the most differentially regulated gene set. Actin cytoskeleton signalling, pyrimidine and purine metabolism pathways were also significantly differentially regulated in CCCs compared with PCCs, whereas all other metabolic pathways were only minimally changed.

were assayed by gene expression microarrays. Gene expression profiling coupled with bioinformatic analyses revealed that the oxidative phosphorylation was the most differentially modulated canonical pathway in CCCs when compared with PCCs, with a significant increase in transcript levels associated with oxidative phosphorylation in CCCs (Fig. 1c,d). The actin cytoskeleton signalling pathway was also differentially regulated in CCCs compared with PCCs (Fig. 1d and Supplementary Fig. 1). We did not observe a significant deregulation in glycolysis/gluconeogenesis, pyruvate metabolism, the TCA cycle, the pentose phosphate pathway, amino sugar metabolism, fatty acid metabolism, fatty acid elongation in the mitochondria, phospholipids degradation, glycine/serine/threonine metabolism, arginine/proline metabolism, phenylalanine metabolism, and valine/leucine/isoleucine metabolism in CCCs compared to PCCs (Fig. 1d and Supplementary Fig. 1).

Quantitative PCR analyses showed specific upregulation of genes associated with mitochondrial biogenesis (*PGC-1 $\alpha$*  (coding for *PGC-1 $\alpha$* ), *PGC-1 $\beta$*  (*PGC-1 $\beta$* ), *Nrf1* and *Esrra* (*ERR $\alpha$* )) and oxidative phosphorylation (*Cox5b*, *Cox4i1* (*Cox4i*), *Atp5a1* (*ATPsynth*) and *Cycs* (*CytC*)) in CCCs compared with PCCs (Fig. 2a). MCCs and PCCs showed similar gene expression levels associated with mitochondria biogenesis and oxidative phosphorylation (Supplementary Fig. 2A), suggestive of a reversible expression of these genes when CCCs are retained in their preferred site of metastasis. The expression levels of some MCC genes were only partially restored to values obtained in PCCs, and this may be due to a collective mixture of MCCs at different stages of metastasis (arrest, extravasation, migration, proliferation). The reversible shift in patterns of metabolic gene expression paralleled that of genes frequently associated with an epithelial-to-mesenchymal transition (EMT) program (Fig. 2a

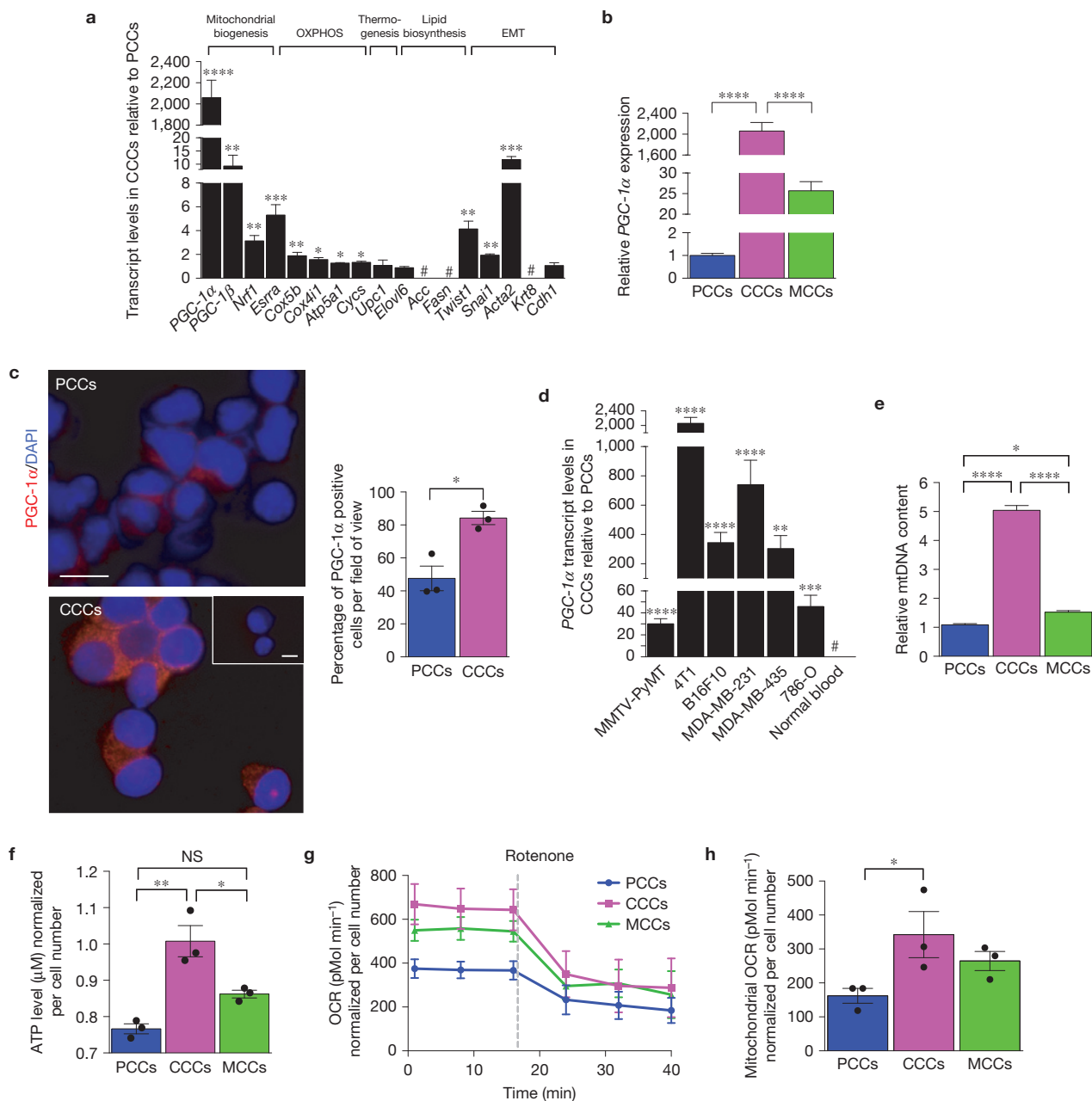


**Figure 2** CCCs exhibit an increased OCR associated with *PGC-1α* expression and mitochondrial biogenesis. **(a)** Quantitative PCR analyses of the relative expression of the indicated genes in CCCs normalized to PCCs. Genes were grouped on the basis of known association with mitochondrial biogenesis, oxidative phosphorylation, thermogenesis, lipid biosynthesis and EMT. #: no transcript was detected ( $n=5$  RNA samples from 5 mice, unpaired two-tailed Student's  $t$ -test). **(b)** Relative *PGC-1α* expression by quantitative PCR analysis in CCCs compared with PCCs in mice with 4T1 orthotopic tumours ( $n=5$  RNA samples from 5 mice, one-way ANOVA). **(c)** Immunostaining for *PGC-1α* of cytospin of PCCs and CCCs and quantification of the relative percentage of *PGC-1α*-positive cells. Scale bars, 10  $\mu\text{m}$ . Nuclear staining (DAPI, blue;  $n=3$  average

percentage of positive cells from 3 mice, unpaired two-tailed Student's  $t$ -test). **(d)** Relative *PGC-1α* expression by quantitative PCR analysis in CCCs compared with PCCs in the indicated orthotopic tumour models. # (normal blood): no *PGC-1α* expression detected ( $n=5$  RNA samples from 5 mice, unpaired two-tailed Student's  $t$ -test). **(e–h)** Mitochondrial DNA (mtDNA) content ( $n=5$  DNA samples from 5 mice, one-way ANOVA; **e**), intracellular ATP levels ( $n=3$  lysates from 3 mice, one-way ANOVA; **f**), OCR (**g**), and mitochondrial OCR (delta OCR pre and post rotenone treatment; **h**) in PCCs, CCCs and MCCs from the 4T1 orthotopic tumour model ( $n=3$  wells of cells from 3 mice, one-way ANOVA). Data are presented as mean  $\pm$  s.e.m. NS, not significant. \* $P < 0.05$ , \*\* $P < 0.01$ , \*\*\* $P < 0.001$ , \*\*\*\* $P < 0.0001$ .

and Supplementary Fig. 2A). Activation of an EMT program is a characteristic feature of invading epithelial cancer cells<sup>8,9</sup>. Mesenchymal genes (*Twist1* (Twist), *Snai1* (Snail) and *Acta2* ( $\alpha$ SMA)) were significantly upregulated in CCCs, whereas epithelial genes

(*Krt8* (CK8) and *Cdh1* (E-cadherin)) were downregulated in CCCs when compared with PCCs and MCCs (Fig. 2a and Supplementary Fig. 2A). Genes associated with thermogenesis, uncoupled respiration (*Ucp1*) and lipid biosynthesis (*Acc*, *Elovl6* and *Fasn*) were unchanged

(Fig. 2a) in CCCs compared to PCCs. Collectively, these results suggest that CCCs assume a characteristic EMT phenotype and transition to a bioenergetic program that uses mitochondrial biogenesis and oxidative phosphorylation.

### PGC-1 $\alpha$ is enriched in CCCs

The enhanced mitochondrial oxidative phosphorylation in CCCs compared with PCCs and MCCs was associated with a marked upregulation of *PGC-1 $\alpha$* , which codes for PGC-1 $\alpha$ , an inducer of mitochondrial biogenesis (Fig. 2a,b). PGC-1 $\alpha$  functions as a master integrator of cellular signals that regulate mitochondrial biogenesis, oxidative phosphorylation, adaptive thermogenesis and fatty acid biosynthesis/degradation<sup>10,11</sup>. PGC-1 $\alpha$  promotes ATP production and energy homeostasis during bioenergetic crises, which renders cells resistant to necrosis and apoptosis<sup>12</sup>. PGC-1 $\alpha$  has been implicated in tumorigenesis<sup>13,14</sup>, yet its function in metastasis remains unknown. *PGC-1 $\alpha$*  expression in CCCs was highest among all other genes known to promote mitochondria biogenesis, including *Esrra*, *Nrf1* and *PGC-1 $\beta$*  (Fig. 2a). Immunostaining for PGC-1 $\alpha$  in PCCs and CCCs shows an increase in the percentage of PGC-1 $\alpha$ <sup>+</sup> CCCs compared with PCCs (Fig. 2c). *PGC-1 $\alpha$*  expression was not detected in peripheral blood cells that were isolated from non-tumour-bearing mice (Fig. 2d). We measured *PGC-1 $\alpha$*  expression levels in CCCs isolated from the MMTV-PyMT spontaneous mouse breast cancer model (these mice spontaneously develop primary mammary tumours that metastasize primarily to the lung<sup>15,16</sup>), as well as in CCCs from mice harbouring a variety of orthotopically implanted tumours, including B16F10 mouse melanoma, MDA-MB-231 (triple-negative human breast cancer cells), MDA-MB-435 human melanoma<sup>17</sup> and 786-O human renal cell carcinoma. In all of the models studied, *PGC-1 $\alpha$*  expression was markedly upregulated in CCCs compared with PCCs (Fig. 2d and Supplementary Fig. 2B,C,E).

To determine whether increased expression of genes associated with mitochondria biogenesis and oxidative phosphorylation in CCCs correlated with increased mitochondria number and mitochondrial respiration, we first measured the oxygen consumption rate (OCR), ATP production and mitochondria DNA content in purified CCCs (Fig. 2e–h). When compared with PCCs, CCCs exhibited an increased mitochondrial DNA content (Fig. 2e), an elevated intracellular ATP levels (Fig. 2f), a higher basal respiration rate (Fig. 2g) and an enhanced mitochondrial OCR (Fig. 2h). The mitochondrial DNA content of CCCs from mice with B16F10 and MDA-MB-231 tumours was also increased (Supplementary Fig. 2D,F). These results suggested that the enhanced oxidative phosphorylation was associated with an increase in the number of mitochondria per cell and that enhanced PGC-1 $\alpha$  expression and mitochondrial biogenesis are features of CCCs.

### PGC-1 $\alpha$ expression facilitates mitochondria biogenesis and invasion of cancer cells

PGC-1 $\alpha$  was silenced (gene expression knockdown, PGC-1 $\alpha$  shRNA) or overexpressed (adenoviral-induced overexpression, Ad. PGC-1 $\alpha$ ) in 4T1, B16F10 and MDA-MB-231 cells (Fig. 3a,b and Supplementary Figs 4A,B and 5A,B). Quantitative PCR analyses revealed significant downregulation of genes associated with mitochondrial biogenesis

(*PGC-1 $\alpha$* , *Nrf1* and *Esrra*) and oxidative phosphorylation (*Cyts* and *Cox5b*) in PGC-1 $\alpha$  shRNA 4T1 cells compared with Scrbl shRNA 4T1 control cells. Genes associated with lipid biosynthesis (*Acc*, *Elovl6* and *Fasn*) and an EMT program (*Krt8*, *Cdh1*, *Twist1*, *Snail* and *Acta2*) were unchanged (Fig. 3a). Induction of PGC-1 $\alpha$  expression reversed the suppression of genes associated with mitochondrial biogenesis and oxidative phosphorylation in PGC-1 $\alpha$  shRNA 4T1 cells, whereas genes associated with lipid biosynthesis remained unchanged (Fig. 3a). A significant reduction in the PGC-1 $\alpha$  transcript and protein levels in 4T1, B16F10 and MDA-MB-231 cells resulted in suppressed mitochondrial biogenesis, as assessed by reduced mitochondrial DNA (Fig. 3c and Supplementary Figs 4C and 5C) and a reduced amount of mitochondrial protein per cell (Fig. 3d and Supplementary Figs 4D and 5D). PGC-1 $\alpha$ -depleted cells exhibited decreased cellular ATP levels (Fig. 3e and Supplementary Figs 4E and 5E). Transmission electron microscopy analyses reveal reduced numbers of mitochondria and swollen mitochondria with disorganized cristae, suggesting impaired mitochondria respiration (Fig. 3f and Supplementary Fig. 3A–D). We verified this by measuring the OCR in a series of mitochondrial stress tests performed on cultured cells. These experiments indicated that mitochondrial respiration capacity was diminished when PGC-1 $\alpha$  was suppressed (Fig. 4a–c and Supplementary Figs 4F and 5F). Specifically, the basal respiration rate was decreased in PGC-1 $\alpha$  shRNA cells compared with Scrbl shRNA control cells ('1' in Fig. 4a). We noted an elevated non-mitochondrial OCR in Scrbl shRNA cells compared with PGC-1 $\alpha$  shRNA cells ('2' in Fig. 4a) following inhibition of electron transport chain (ETC) complex I+II (rotenone + atpenin A5 treatments). Targeted mass spectrometry and metabolomics analyses<sup>18</sup> of PGC-1 $\alpha$  shRNA 4T1 cells compared with Scrbl shRNA 4T1 cells revealed lower levels of some of the metabolite levels associated with glycolysis, the TCA cycle, amino sugar metabolism, pyruvate metabolism, phospholipid metabolism, pyrimidine and purine metabolism, and some of these associated metabolites showed elevated levels (Supplementary Fig. 6A). Metabolomics analyses of PGC-1 $\alpha$  shRNA 4T1 cells cultured using <sup>13</sup>C-labelled glucose also showed insignificant differences in the accumulation rate of glycolytic/gluconeogenic metabolites when compared with Scrbl shRNA control cells (Supplementary Fig. 7A). OCR measurements also revealed a decreased capacity for ATP-coupled OCR in PGC-1 $\alpha$  shRNA cells compared with Scrbl shRNA control cells (B' < B in Fig. 4b) and an enhanced proton leak (C' > C in Fig. 4b). PGC-1 $\alpha$  shRNA cells respire at their maximal capacity (D' < A in PGC-1 $\alpha$  shRNA cells versus D > A in Scrbl shRNA cells in Fig. 4b), possibly to compensate for the loss in ATP-coupled respiration subsequent to the loss of mitochondria, lowering the basal respiration rate. Mitochondrial OCR was decreased in PGC-1 $\alpha$  shRNA cells compared with Scrbl shRNA cells, which also occurred when either complex I or complex I+II of the ETC was inhibited (Fig. 4c). Compensation through complex II activity is not observed when mitochondrial respiration is compromised by suppression of PGC-1 $\alpha$  in live cells; however, OCR measurements of permeabilized cells suggest a possible differential regulation of complex-II-linked OCR activity (increased OCR following succinate injection) in PGC-1 $\alpha$  shRNA cells compared with Scrbl shRNA cells (Fig. 4d). These results indicate that PGC-1 $\alpha$  modulates mitochondrial biogenesis in cancer cells without significantly affecting

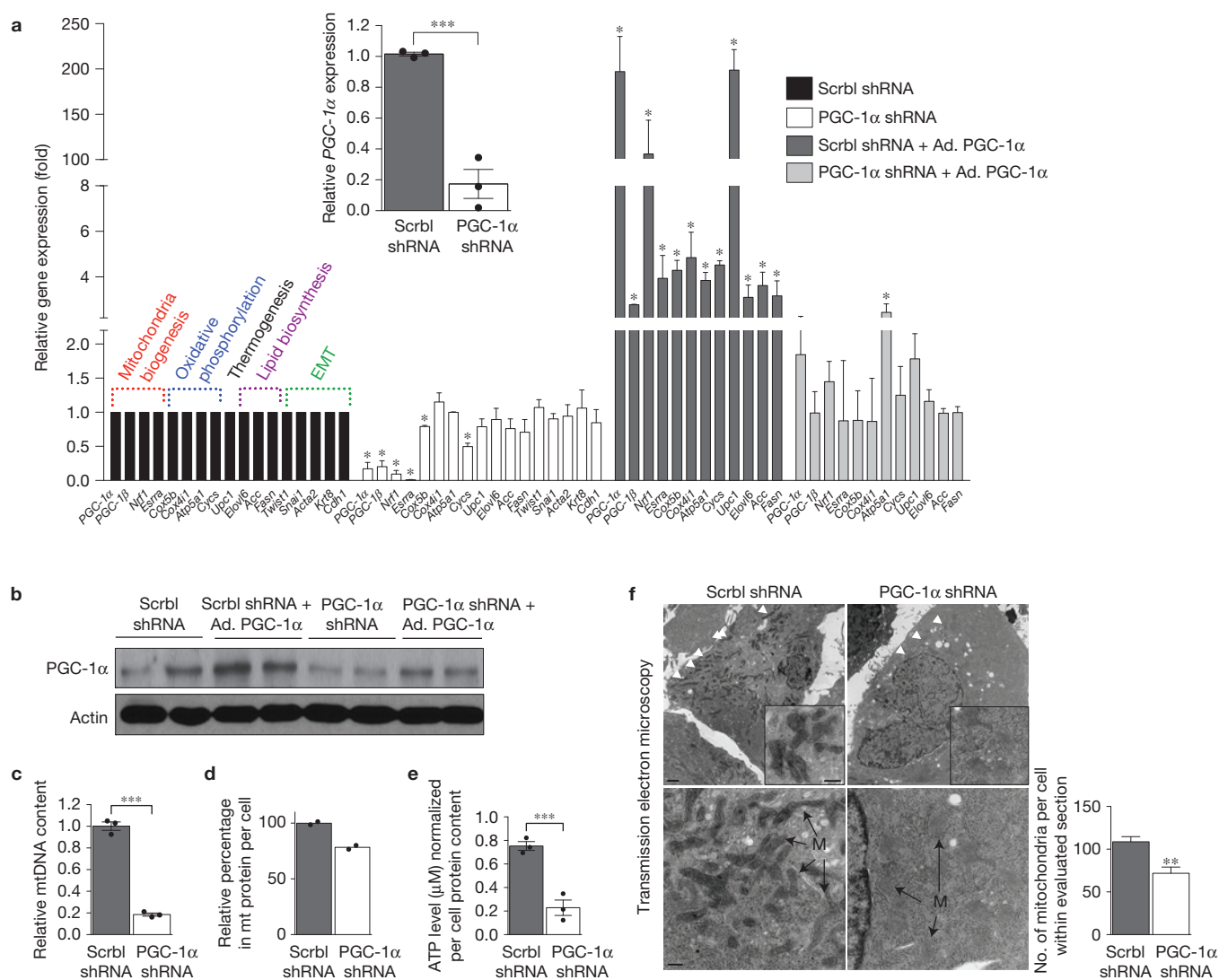


**Figure 3** PGC-1 $\alpha$  expression is associated with mitochondrial respiration and biogenesis in cancer cells. **(a)** Real-time PCR analyses of the relative expression of the indicated genes in PGC-1 $\alpha$  shRNA 4T1 cells normalized to Scrbl shRNA 4T1 cells, and PGC-1 $\alpha$  shRNA 4T1 and Scrbl shRNA 4T1 cells with adenoviral overexpression of PGC-1 $\alpha$  (Ad. PGC-1 $\alpha$ ), also normalized to Scrbl shRNA 4T1 cells (arbitrarily set to 1). The inset shows PGC-1 $\alpha$  expression specifically in Scrbl shRNA 4T1 and PGC-1 $\alpha$  shRNA 4T1 cells ( $n=3$  RNA samples from cells, unpaired two-tailed Student's  $t$ -test). **(b)** Western blot for PGC-1 $\alpha$  in indicated cells/treatments. Uncropped images of blots are shown in Supplementary Fig. 9. **(c,d)** Mitochondrial DNA (mtDNA) content ( $n=3$  DNA samples from cells, unpaired two-tailed

Student's  $t$ -test; **(e)** and mitochondrial protein content relative to total cell protein content **(d)** in PGC-1 $\alpha$  shRNA 4T1 cells normalized to Scrbl shRNA 4T1 cells ( $n=2$  extracted cell lysates). **(e)** Intracellular ATP levels in PGC-1 $\alpha$  shRNA 4T1 cells normalized to Scrbl shRNA 4T1 cells ( $n=3$ , unpaired two-tailed Student's  $t$ -test). **(f)** Transmission electron microscopy of 4T1 Scrbl shRNA and PGC-1 $\alpha$  shRNA, white arrowheads and 'M' identify mitochondria. Scale bars upper panel: 2  $\mu$ m; inset and lower panel: 500 nm. Quantification of the number of mitochondria per cell in the imaged section (Scrbl shRNA,  $n=9$  cells; PGC-1 $\alpha$  shRNA,  $n=6$  cells, unpaired two-tailed Student's  $t$ -test). Data are presented as mean  $\pm$  s.e.m. \* $P < 0.05$ , \*\* $P < 0.01$ , \*\*\* $P < 0.001$ .

glycolysis. These results also suggest that PGC-1 $\alpha$  suppression impacts the oxidative phosphorylation capacity of cancer cells by both suppressing mitochondrial biogenesis and directly impacting ATP-coupled respiration and the efficacy of the ETC within the remaining mitochondrial pool. The transition from PCCs to CCCs seems to be associated with enhanced reliance on mitochondrial respiration, which is probably mediated, in part, by PGC-1 $\alpha$ . PGC-1 $\beta$ , *Esrra* and *Nrf1* were upregulated in CCCs (Fig. 2a) and downregulated when PGC-1 $\alpha$  was suppressed (Fig. 3a), highlighting an upstream action of PGC-1 $\alpha$  in this setting<sup>19</sup>.

### PGC-1 $\alpha$ expression determines the invasive capacity and metastasis potential of cancer cells

Next, we investigated whether PGC-1 $\alpha$ -mediated induction of mitochondria biogenesis and respiration was associated with the invasive capacity of CCCs. We measured invasion, migration and cell division of 4T1, B16F10 and MDA-MB-231 cells with stable suppression, rescued expression or overexpression of PGC-1 $\alpha$ , or with rotenone treatment. Suppression of PGC-1 $\alpha$  revealed specific downregulation of mitochondrial respiration, but overexpression of PGC-1 $\alpha$  in cancer cells resulted in a mixed metabolic response, probably resulting

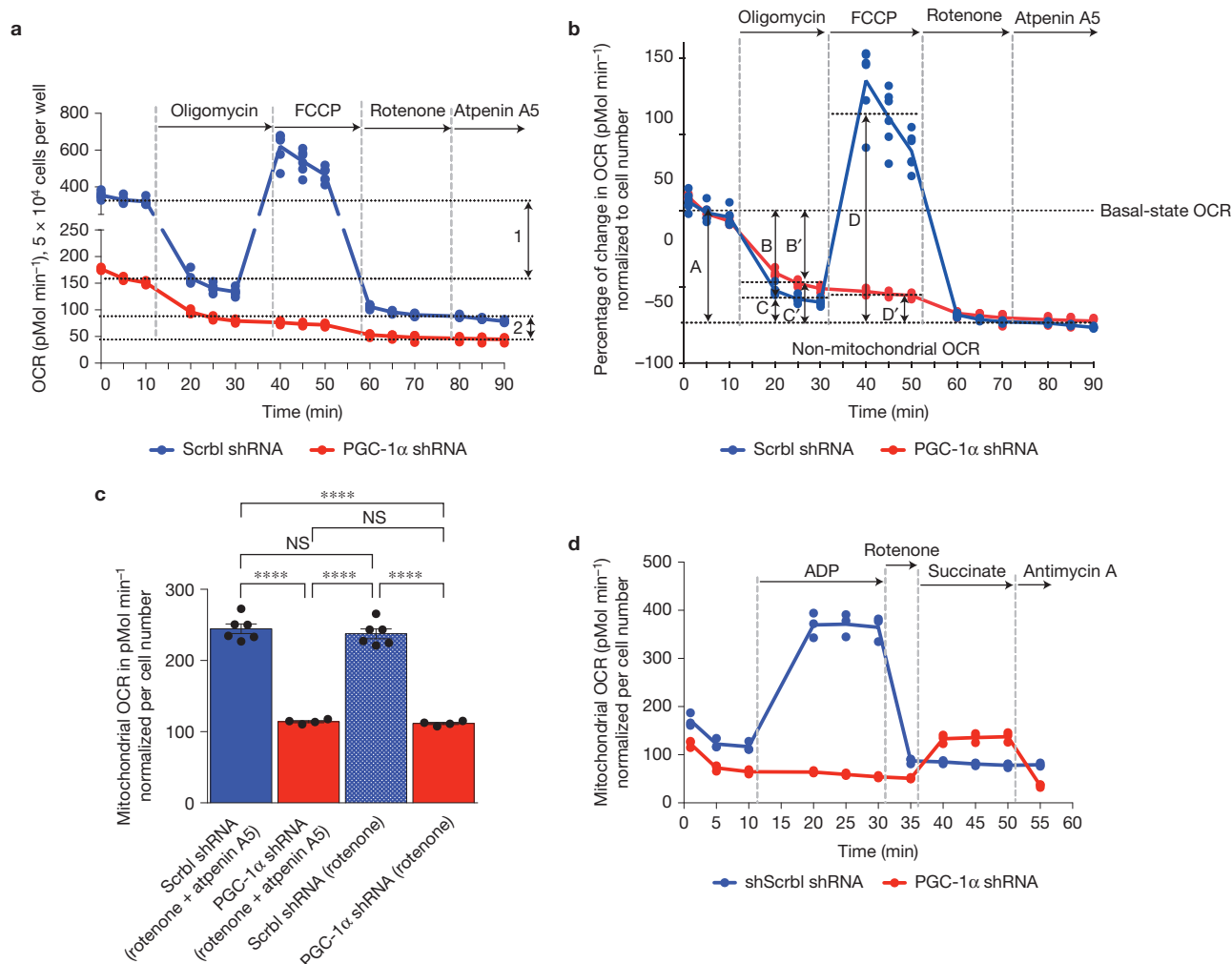


**Figure 4** PGC-1 $\alpha$  expression modulates complex-I-driven oxidative phosphorylation in 4T1 cancer cells. **(a)** Relative OCR normalized to cell number over time in PGC-1 $\alpha$  shRNA 4T1 ( $n=4$  wells) and Scrbl shRNA 4T1 ( $n=6$  wells) cells. 1: differential basal state OCR; 2: differential non-mitochondrial OCR. **(b)** Percentage change in OCR normalized per cell number in PGC-1 $\alpha$  shRNA 4T1 ( $n=4$  wells) and Scrbl shRNA 4T1 ( $n=6$  wells) cells. A: initial OCR; B and B': percentage of OCR used for ATP synthesis in Scrbl shRNA 4T1 and PGC-1 $\alpha$  shRNA 4T1 cells respectively; C and C': percentage of

OCR associated with proton leakage in Scrbl shRNA 4T1 and PGC-1 $\alpha$  shRNA 4T1 cells respectively; D and D': maximum mitochondria respiratory capacity of Scrbl shRNA 4T1 and PGC-1 $\alpha$  shRNA 4T1 cells respectively. **(c)** Mitochondrial OCR (delta OCR pre and post rotenone with or without atpenin A5 treatment) in PGC-1 $\alpha$  shRNA 4T1 ( $n=4$ ) and Scrbl shRNA 4T1 ( $n=6$  wells) cells, one-way ANOVA. **(d)** OCR measurements in permeabilized 4T1 Scrbl shRNA and PGC-1 $\alpha$  shRNA cells ( $n=3$  wells per cell line). Data are presented as mean  $\pm$  s.e.m. NS, not significant. \*\*\*\* $P < 0.0001$ .

from the hyper induction of many metabolic processes due to supra-physiological levels of PGC-1 $\alpha$  in cultured cells<sup>12</sup> (Fig. 3a). Nevertheless, overexpression of PGC-1 $\alpha$  in PGC-1 $\alpha$  shRNA cancer cells partially reversed the gene expression pattern associated with suppression of mitochondrial biogenesis and respiration (Fig. 3a). PGC-1 $\alpha$  knockdown and rotenone treatment significantly reduced invasion of cancer cells, and overexpression of PGC-1 $\alpha$  enhanced invasion and restored invasive properties to PGC-1 $\alpha$  shRNA cells (Fig. 5a,b and Supplementary Figs 3E, 4G,H and 5G,H). Migration was also dependent on PGC-1 $\alpha$  expression levels (Fig. 5c,d and Supplementary Figs 3E, 4I,J and 5I,J), whereas alterations in PGC-1 $\alpha$  expression had no effect on cell division (Fig. 5e). Loss of PGC-1 $\alpha$  expression reduced the ability of cancer cells to tighten type I collagen in contraction assays, suggestive of compromised actin cytoskeleton remodelling and associated ATP-fuelled molecular motors (Fig. 5f and Supplementary

Figs 4K and 5K). Overexpression of PGC-1 $\alpha$  alone did not enhance collagen I contraction, but rescued PGC-1 $\alpha$  shRNA reduced type I collagen contractility (Fig. 5f and Supplementary Figs 4K and 5K). Taken together, these results indicate that loss of PGC-1 $\alpha$  expression diminishes invasive and migratory properties of cancer cells and these features are restored with the rescue of PGC-1 $\alpha$  gene expression in PGC-1 $\alpha$  shRNA cancer cells.

### PGC-1 $\alpha$ promotes cancer cell metastasis

Suppression of PGC-1 $\alpha$  expression had no effect on the growth of primary 4T1 tumours (Fig. 6a,b). PGC-1 $\alpha$  shRNA MDA-MB-231 tumours showed similar tumour growth kinetics and weight when compared to control Scrbl shRNA MDA-MB-231 tumours (Supplementary Fig. 8A,B). Similarly, PGC-1 $\alpha$  gene expression knockdown did not impact the growth of primary B16F10 melanomas

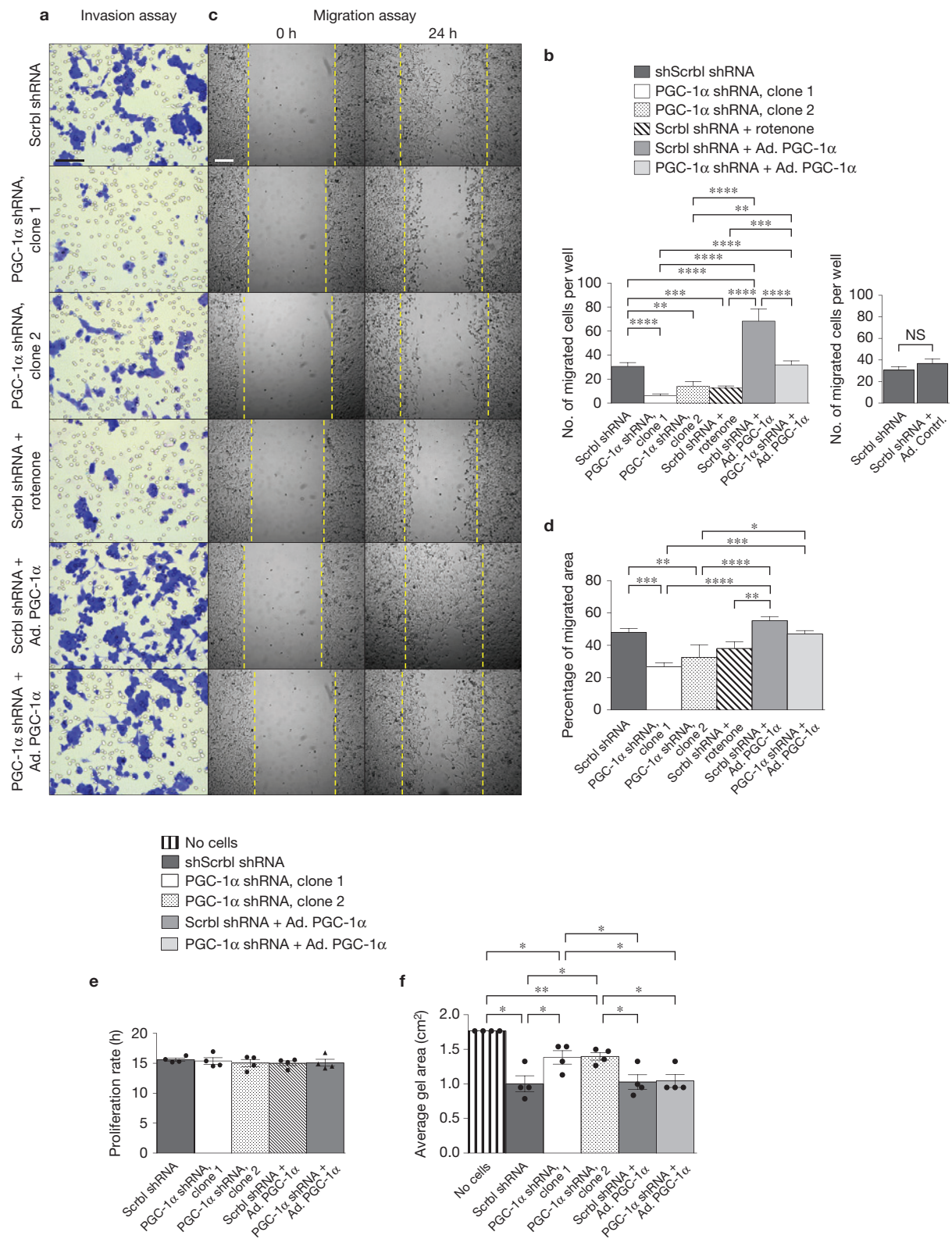


**Figure 5** PGC-1 $\alpha$  expression modulates cancer cell invasion and migration. **(a)** Haematoxylin-stained 4T1 cells (scale bar, 50  $\mu$ m) following invasion. **(b)** Quantification of invasion assay. Ad. PGC-1 $\alpha$ : adenoviral induction of PGC-1 $\alpha$  expression ( $n=6$  wells per group, one-way ANOVA). Ad. Contrl: adenovirus with empty pcDNA vector control ( $n=6$  wells per group, unpaired two-tailed Student's  $t$ -test). **(c)** Light microscopy imaging (scale bar, 50  $\mu$ m) of migrated

cells in scratch assay. **(d)** Quantification of migration assay ( $n=5$  wells per group, one-way ANOVA). **(e)** Proliferation rate ( $n=4$  cell count measurements over time per group, one-way ANOVA). **(f)** Type I collagen gel area reflecting gel contraction by indicated cells ( $n=4$  wells per group, unpaired two-tailed Student's  $t$ -test). Data are presented as mean  $\pm$  s.e.m. NS, not significant. \* $P < 0.05$ , \*\* $P < 0.01$ , \*\*\* $P < 0.001$ , \*\*\*\* $P < 0.0001$ .

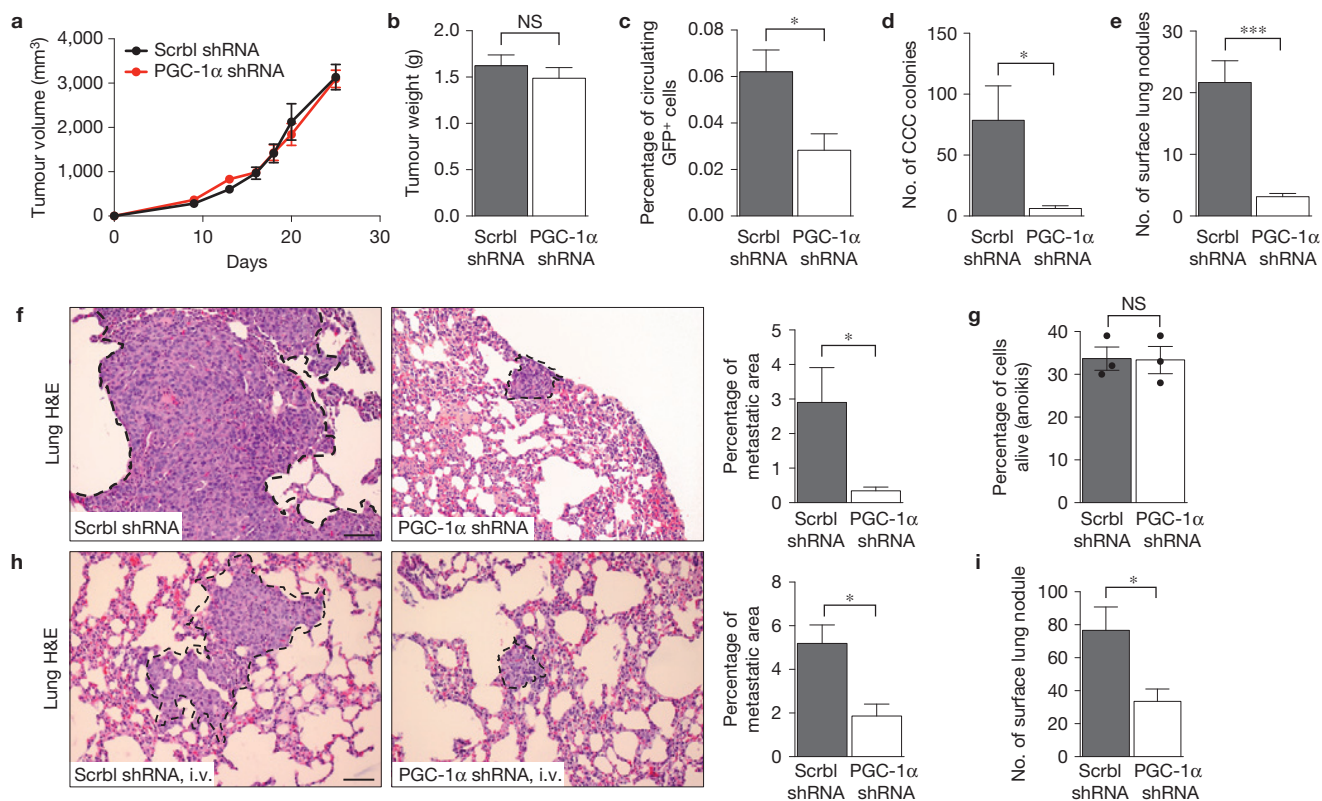


**Figure 6** Suppression of *PGC-1α* expression suppresses cancer cell dissemination and metastasis. **(a)** Scrbl shRNA 4T1 and PGC-1α shRNA 4T1 cells were implanted in the mammary fat pad of mice and tumour volume was measured over time (Scrbl shRNA 4T1,  $n=6$  mice; PGC-1α shRNA 4T1,  $n=7$  mice). **(b)** Tumour weight at experimental endpoint (Scrbl shRNA 4T1,  $n=6$  mice; PGC-1α shRNA 4T1,  $n=7$  mice, unpaired two-tailed Student's *t*-test). **(c)** Percentage of GFP<sup>+</sup> cancer cells per 200 μl blood collected at experimental endpoint (Scrbl shRNA 4T1,  $n=6$  mice; PGC-1α shRNA 4T1,  $n=6$  mice, unpaired two-tailed Student's *t*-test). **(d)** Number of CCC colonies formed (Scrbl shRNA 4T1,  $n=6$  mice; PGC-1α shRNA 4T1,  $n=7$  mice, unpaired two-tailed Student's *t*-test). **(e)** Number of lung surface nodules in mice with orthotopic Scrbl shRNA 4T1 and PGC-1α shRNA 4T1 tumours (Scrbl shRNA 4T1,  $n=6$  mice; PGC-1α shRNA 4T1,  $n=7$  mice, unpaired two-tailed Student's *t*-test). **(f)** Representative images of H&E-stained lung

sections of mice harbouring orthotopic Scrbl shRNA 4T1 and PGC-1α shRNA 4T1 tumours and percentage of metastatic lung surface area relative to total lung surface area. Scale bar, 50 μm. Metastatic lung nodules are circled (Scrbl shRNA 4T1,  $n=6$  mice; PGC-1α shRNA 4T1,  $n=7$  mice, unpaired two-tailed Student's *t*-test). **(g)** Percentage of alive cells in anoikis assay ( $n=3$  average percentage of live-cell measurements, unpaired two-tailed Student's *t*-test). **(h)** Representative images of H&E-stained lung sections of mice with intravenous injection of Scrbl shRNA 4T1 and PGC-1α shRNA 4T1 cells and percentage of metastatic lung surface area relative to total lung surface area (Scrbl shRNA 4T1,  $n=5$  mice; PGC-1α shRNA 4T1,  $n=6$  mice, unpaired two-tailed Student's *t*-test). Scale bar, 50 μm. Lung nodules are circled. **(i)** Number of lung surface nodules (Scrbl shRNA 4T1,  $n=5$  mice; PGC-1α shRNA 4T1,  $n=6$  mice, unpaired two-tailed Student's *t*-test). Data are presented as mean ± s.e.m. NS, not significant. \* $P < 0.05$ , \*\*\* $P < 0.001$ .

(Supplementary Fig. 8I,J). The number of CCCs was significantly reduced in mice with PGC-1α shRNA 4T1 tumours compared with mice with control Scrbl shRNA 4T1, as assessed by the reduced number of GFP<sup>+</sup> cancer cells in the blood by FACS analysis and also by the decreased number of blood-derived cancer cell colonies (colony formation assay; Fig. 6c,d). The decreased dissemination of cancer cells was associated with a significant reduction in the computed percentage of metastatic lung area and the number of surface lung nodules of mice with PGC-1α shRNA 4T1 tumours compared with mice with control Scrbl shRNA 4T1 tumours (Fig. 6e,f). These findings were reproduced using a second knockdown clone of PGC-1α in 4T1 cells (Supplementary Fig. 7B–E). CCC numbers (Supplementary Fig. 8C,D) and metastasis (Supplementary Fig. 8E,F) were also significantly reduced in mice bearing PGC-1α shRNA MDA-MB-231 tumours in contrast with mice bearing Scrbl shRNA MD-MB-231 tumours. Decreased cancer cell dissemination and reduced metastatic disease were also observed when PGC-1α expression was

suppressed in B16F10 melanoma cells (Supplementary Fig. 8K–N). These results indicate that suppression of PGC-1α reduces cancer cell metastasis.

Our studies pointed to the possibility that PGC-1α expression is essential for intravasation of the cancer cells into the circulation. Similar anchorage-independent survival (anoikis) rates in cells with suppressed PGC-1α was observed compared with control lines (Fig. 6g). We next investigated whether extravasation of cancer cells is similarly impaired when PGC-1α is suppressed. We monitored lung colonization and lung metastatic nodule formation in mice following intravenous injection of PGC-1α shRNA and control Scrbl shRNA cells. Metastatic lung colonization and nodule formation were significantly impaired when PGC-1α expression was suppressed (Fig. 6h,i and Supplementary Fig. 8G,H,O,P). Taken together, our results support an important role for PGC-1α-mediated mitochondrial biogenesis and oxidative phosphorylation in facilitating migration, invasion and intravasation/extravasation of cancer cells.

### Mitochondrial respiration fuels cancer cell motility

To evaluate PGC-1 $\alpha$  expression in invading cancer cells *in vivo*, we FACS-purified PCCs on the basis of GFP expression and  $\alpha$ SMA labelling. Cancer cells exhibiting an EMT program (GFP<sup>+</sup>/ $\alpha$ SMA<sup>+</sup>) express significantly higher levels of PGC-1 $\alpha$  when compared with cancer cells without an EMT program (GFP<sup>+</sup>/ $\alpha$ SMA<sup>-</sup>) (Fig. 7a). Hypoxia is a potent inducer of the invasive properties of cancer cells, and thus we evaluated PGC-1 $\alpha$  expression in 4T1, B16F10 and MDA-MB-231 cells following re-oxygenation from hypoxia. PGC-1 $\alpha$  expression was significantly increased following re-oxygenation (Fig. 7b). Cells in hypoxia as well as after re-oxygenation showed elevated PGC-1 $\alpha$  and Twist expression (Fig. 7c). However, when PGC-1 $\alpha$  was suppressed, hypoxia had no effect on PGC-1 $\alpha$  expression, but did upregulate Twist1 expression, suggesting that Twist1 expression associated with hypoxia-induced EMT was independent of PGC-1 $\alpha$  upregulation (Fig. 7c). Similarly, in cells with knockdown of Twist1 expression, PGC-1 $\alpha$  expression was elevated under hypoxic conditions, whereas Twist1 was not upregulated (Fig. 7c). Furthermore, double immunolabelling for CK8 (epithelial marker, *Krt8*) and  $\alpha$ SMA (mesenchymal marker, *Acta2*) revealed a similar number of double-positive cancer cells in PGC-1 $\alpha$  shRNA and control Scrl shRNA primary tumours, suggesting an equal frequency of cancer cells acquiring an EMT program (Fig. 7d). Quantitative PCR analyses for mesenchymal and epithelial genes showed comparable levels of EMT-program-related genes in both PGC-1 $\alpha$  shRNA and control Scrl shRNA primary tumours (Fig. 7e). Immunolabelling for Twist1 and PGC-1 $\alpha$  in CCCs indicated that most of the CCCs were PGC-1 $\alpha$ <sup>+</sup>, and nearly all PGC-1 $\alpha$ <sup>+</sup> CCCs were Twist<sup>+</sup> (Fig. 7f). Taken together these results suggest that acquisition of an EMT and invasive phenotype is associated with Twist1 expression, and that PGC-1 $\alpha$  upregulation in invasive cells is independent of Twist1 upregulation. The invasive feature of migrating cancer cells, which may be precipitated by hypoxia, was associated with elevated PGC-1 $\alpha$  expression; however, suppression of PGC-1 $\alpha$  did not impact the expression of EMT-related genes (Fig. 3a). Collectively, these findings suggest that induction of PGC-1 $\alpha$  expression is not mutually exclusive to the acquisition of mesenchymal features (EMT), and modulating mitochondrial respiration in cancer cells through hypoxia-driven induction of PGC-1 $\alpha$  expression does not limit the induction of EMT-associated genes, but functionally impairs cell motility and invasive properties.

### Enhanced PGC-1 $\alpha$ expression is associated with distant metastasis and poor outcome in patients with invasive breast cancer

We measured PGC-1 $\alpha$  gene expression in laser-microdissected neoplastic cells collected from the periphery of breast tumours in patients diagnosed with invasive ductal carcinomas (IDCs; further categorized on the basis of the presence of disseminated tumour cells (DTCs) in the bone marrow (BM<sup>+</sup>: positive DTC detection,  $n = 14$ ; BM<sup>-</sup>: negative DTC detection,  $n = 16$ ); ref. 20). High PGC-1 $\alpha$  transcript levels in cancer cells were significantly correlated with positive DTC status (Fig. 8a and Supplementary Table 1). These data suggest a possible role for PGC-1 $\alpha$  in mediating cancer cell dissemination to the bone in patients with IDCs.

We next probed tissue microarrays for the expression of PGC-1 $\alpha$  in breast tumours from 161 patients with IDCs (Fig. 8b and Supplementary Table 2). There was a significant correlation between high PGC-1 $\alpha$  expression at the invasive tumour front and distant metastasis and, moreover, poor overall and cancer-specific survival (Fig. 8c,d). We also detected PGC-1 $\alpha$  expression in CCCs ('CTCs') collected from patients with metastatic IDCs, and PGC-1 $\alpha$ <sup>+</sup> CTCs were negative for the leukocyte marker CD45 (Fig. 8e and Supplementary Table 3). In addition, CTCs were detected in 11 out of 13 patients with IDCs who had confirmed lung metastases and more than 80% of the CTCs were PGC-1 $\alpha$ <sup>+</sup> (Fig. 8f and Supplementary Table 4). These results illustrate a positive correlation between PGC-1 $\alpha$  expression and the formation of distant metastases in patients with invasive breast cancer.

### DISCUSSION

New therapeutic strategies are beginning to focus on the unique patterns of metabolism observed in cancer cells. Therefore, determining the metabolic requirements of invasive cancer cells could be of therapeutic value. We show that the PGC-1 $\alpha$ -mediated mitochondrial biogenesis and respiration in cancer cells is functionally relevant for metastatic dissemination. Invading cancer cells rely on PGC-1 $\alpha$  to stimulate mitochondrial biogenesis and oxidative phosphorylation during their transit to target organs of metastasis. Indeed, PGC-1 $\alpha$  suppression significantly impaired mitochondrial biogenesis and oxidative phosphorylation and, moreover, decreased the frequency of metastasis. The enhanced mitochondrial respiration/oxidative phosphorylation did not impact glycolytic and anabolic rates in the CCCs, and did not affect cancer cell proliferation or primary tumour growth kinetics. Although more studies are required to specifically connect PGC-1 $\alpha$ -induced oxidative phosphorylation and metastasis, these results demonstrate that invasive and migratory properties of cancer cells are dependent on mitochondrial respiration and identify PGC-1 $\alpha$  as a potential target for therapeutic intervention.

Mitochondrial proficiency and detoxification of reactive oxygen species (ROS) are critical for cancer cell viability<sup>21,22</sup>. Although diminished oxygen levels feed back to reduce mitochondrial biogenesis to avoid metabolic crisis in normal cells<sup>3,4</sup>, zonal hypoxia and focal nutrient bioavailability in different areas of a growing tumour can differentially impact the energetic needs of cancer cells. ROS accumulation in hypoxic cancer cells induces expression of PGC-1 $\alpha$ / $\beta$  to promote detoxification through direct induction of superoxide dismutase 2 (SOD2), catalase and glutathione peroxidase<sup>23-25</sup>. Focal hypoxia may induce an EMT program<sup>16,26</sup>, and our results indicate that although cancer cells acquire a mesenchymal phenotype (EMT) independently of PGC-1 $\alpha$ -induced pathways, both pathways coexist and are associated with cancer cell migration, invasion and metastasis<sup>27</sup>. We propose that a functional EMT program in cancer cells, with acquisition of enhanced migratory and invasive properties, is synergistically coupled with mitochondrial biogenesis and respiration. Altering mitochondrial function could also impact other fundamental cellular processes, in part through retrograde mitochondria–nucleus signalling, and contribute to changes in the nuclear transcriptome associated with survival and acquisition of cancer stem cell properties<sup>28</sup>. In addition, dynamic changes in the

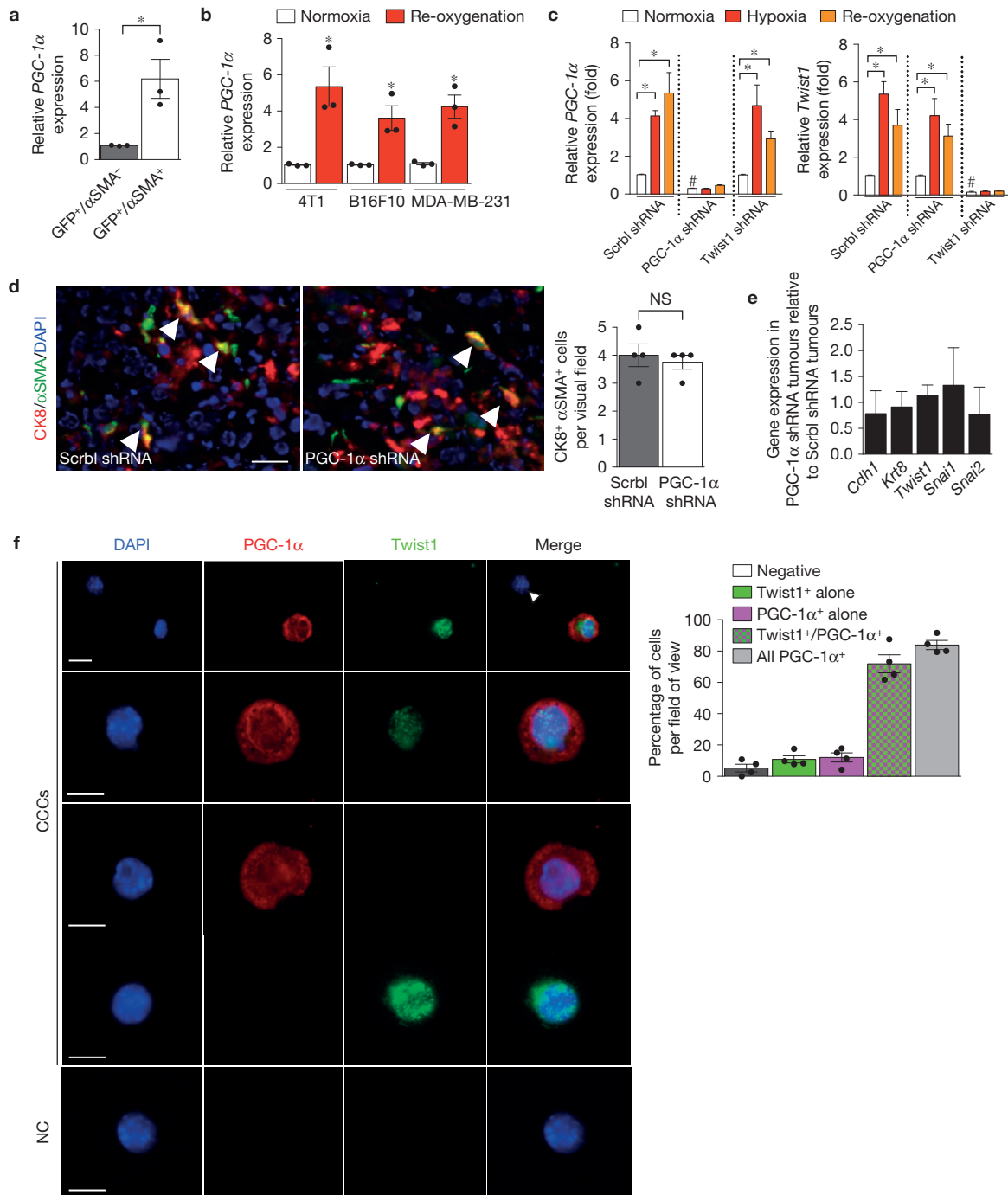


**Figure 7** PGC-1 $\alpha$  expression is co-induced with an EMT program. **(a)** PGC-1 $\alpha$  expression in FACS-purified GFP<sup>+</sup>/ $\alpha$ SMA<sup>-</sup> and GFP<sup>+</sup>/ $\alpha$ SMA<sup>+</sup> cells from 4T1 primary tumours ( $n=3$  RNA samples from FACS-purified cells of 3 mice, unpaired two-tailed Student's  $t$ -test). \* $P < 0.05$ . **(b)** PGC-1 $\alpha$  expression in the indicated cells cultured in normoxia and re-oxygenated (24 h) following 48 h of hypoxia ( $n=3$  RNA samples per cell line, unpaired two-tailed Student's  $t$ -test). \* $P < 0.05$ . **(c)** PGC-1 $\alpha$  and Twist1 expression in Scrbl shRNA 4T1, PGC-1 $\alpha$  shRNA 4T1 and Twist1 shRNA 4T1 cells cultured in normoxia, hypoxia (48 h), and re-oxygenated (24 h) following 48 h of hypoxia ( $n=3$  RNA samples per cell line, unpaired two-tailed Student's  $t$ -test). \* $P < 0.05$ . # $P < 0.05$  for PGC-1 $\alpha$  expression in PGC-1 $\alpha$  shRNA 4T1 compared with Scrbl shRNA 4T1 in normoxic conditions, and for Twist1 expression in Twist1 shRNA 4T1 compared with Scrbl shRNA 4T1 in normoxic conditions. **(d)** Representative CK8 (red) and  $\alpha$ SMA (green) immunolabelling of the

primary tumour. Nuclear staining (DAPI, blue). Arrowheads point to double-positive (CK8<sup>+</sup>/ $\alpha$ SMA<sup>+</sup>) cells. Scale bar, 100  $\mu$ m. Bar graph: quantification of number of CK8<sup>+</sup>/ $\alpha$ SMA<sup>+</sup> cells per field of view ( $n=4$  stained slides of tumours from 4 mice, unpaired two-tailed Student's  $t$ -test). **(e)** Relative expression of the indicated genes in PGC-1 $\alpha$  shRNA 4T1 tumours normalized to Scrbl shRNA 4T1 tumours ( $n=5$  RNA samples from tumours of 5 mice, unpaired two-tailed Student's  $t$ -test). **(f)** Immunolabelling of cytopsin of 4T1 CCCs for Twist1 and PGC-1 $\alpha$  ( $n=4$  mice). Scale bars, 10  $\mu$ m. NC: negative control, only secondary antibody used. Bar graph: Relative percentage of CCCs negative for both Twist1 and PGC-1 $\alpha$ , positive for Twist1 alone (PGC-1 $\alpha$ <sup>-</sup>), positive for PGC-1 $\alpha$  alone (Twist1<sup>-</sup>), positive for both Twist1 and PGC-1 $\alpha$ , and all PGC-1 $\alpha$ -positive CCCs (regardless of Twist1 status). Scale bars, 25  $\mu$ m (upper panel), 10  $\mu$ m (lower panel). Data are presented as mean  $\pm$  s.e.m. NS, not significant.

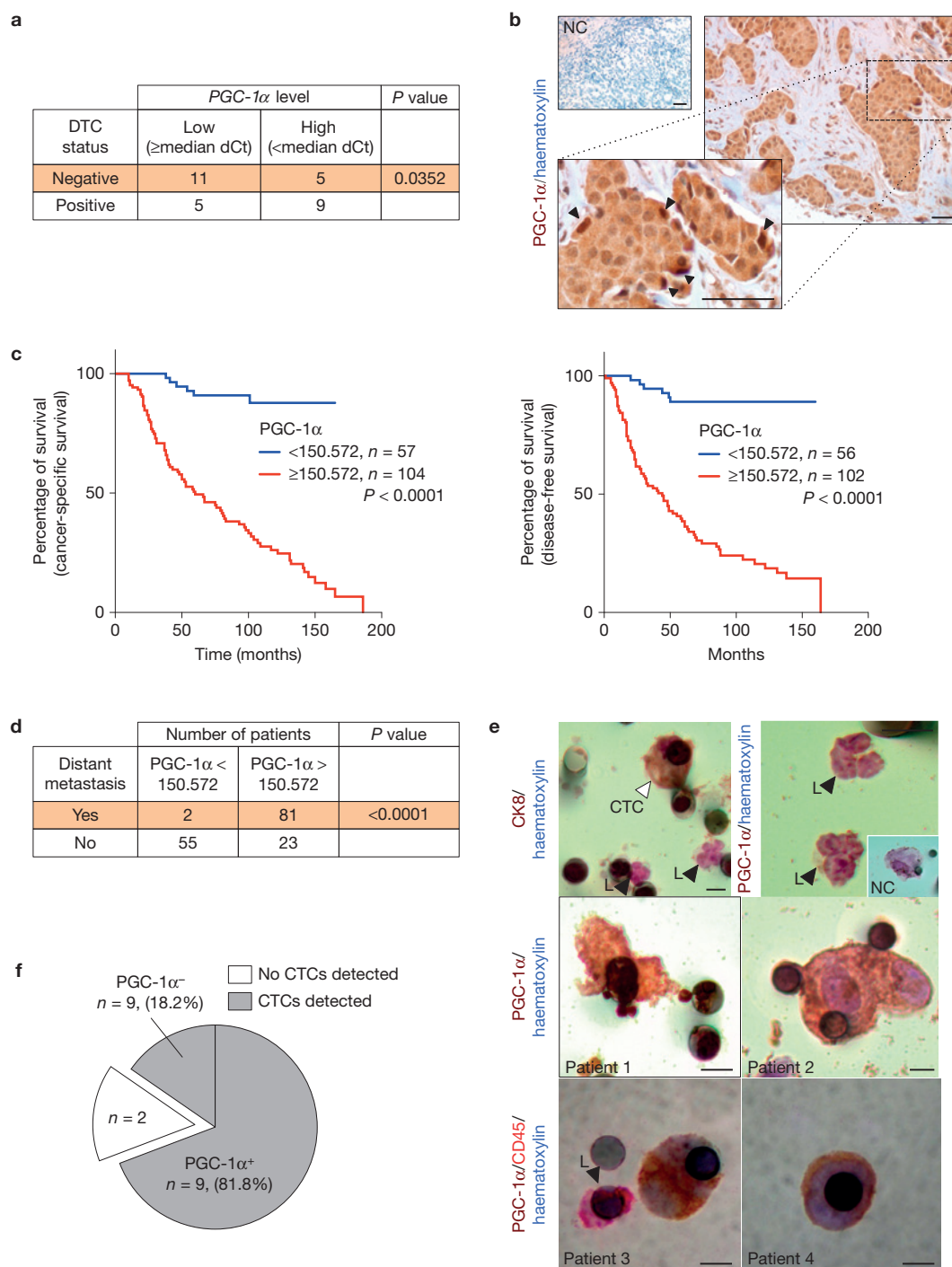


**Figure 8** PGC-1 $\alpha$  expression in CCCs correlates with invasion and distant metastasis in patients with IDCs. **(a)** Correlation of relative PGC-1 $\alpha$  expression (median dCt value used as cut-off) in laser-dissected neoplastic cells from resected tumours of patients with IDCs and status of DTCs in the bone marrow (BM<sup>+</sup>: bone marrow is positive for DTCs; BM<sup>-</sup>: bone marrow is negative for DTCs). BM<sup>+</sup> status,  $n=16$  RNA samples from 16 patients; BM<sup>-</sup> status,  $n=14$  RNA samples from 14 patients. (Supplementary Table 1, one-sided  $\chi^2$  analysis). **(b)** Immunohistochemistry staining for PGC-1 $\alpha$  (haematoxylin counter stain) in breast tumours from patients with IDCs. NC: negative control, only secondary antibody and haematoxylin counter stain. Arrowheads in the zoomed-in inset point to the strongly positive PGC-1 $\alpha$  cells found on the invasive edge. Scale bar, 50  $\mu$ m. **(c)** Cancer-specific survival and disease-free survival of IDC patients grouped on the basis of PGC-1 $\alpha$  expression

(Supplementary Table 2, log-rank test). **(d)** Correlative analysis of the number of IDC patients with and without distant metastases categorized on the basis of the indicated PGC-1 $\alpha$  expression threshold (Supplementary Table 2, Fisher's exact test). Kaplan-Meier curves were drawn and differences between the curves were calculated by the log-rank test. **(e)** A circulating cancer cell ('CTC', right arrowhead) stains for the epithelial marker CK8, whereas leukocytes ('L', left arrowhead) are negative for CK8 (upper left panel). Leukocytes are negative for PGC-1 $\alpha$  (upper right panel). Inset shows negative control (NC) staining of a CTC (secondary antibody alone). PGC-1 $\alpha$  (patient 1 and 2) or CD45 and PGC-1 $\alpha$  (patient 3 and 4) immunostaining of CTCs (lower panels, Supplementary Table 3). Scale bars, 8  $\mu$ m. **(f)** Representation of the PGC-1 $\alpha$ <sup>+</sup> CTC status evaluated by immunohistochemistry staining in IDC patients with lung metastasis (Supplementary Table 4).

energy processing of cancer cells in disease progression probably impact the surrounding tumour stroma, which in turn may impact the migratory phenotype of cells.

We speculate that cells in the hypoxic areas of the tumour trigger acquisition of migratory features through EMT and PGC-1 $\alpha$ -mediated mitochondrial respiration. It is conceivable that invading cancer cells enhance their mitochondrial content and upregulate oxidative phosphorylation as they approach more oxygenated areas of the tumour, which ensures the increased production of ATP required for trafficking to distal tissues. Mitochondrial proficiency and ROS detoxification are critical for cancer cell viability<sup>21,22</sup>, and ATP generation (a feature of non-dividing migratory cells<sup>3,29</sup>) and antioxidant production ensure cancer cell survival when detaching from their basement membrane<sup>30</sup>. The high ATP production found in CCCs may be used to promote their retention in target organs. A recent study showed that ATP secreted from platelets stimulates endothelial cell retraction that promotes transendothelial migration of cancer cells<sup>31</sup>.

Our clinical analysis of human invasive breast cancers revealed a significant correlation between PGC-1 $\alpha$  expression in invasive cancer cells and formation of distant metastases. Of note, expression of ERR $\alpha$  (PGC-1 $\alpha$ -coupled transcription factor) in IDC patients also correlates with poor prognosis<sup>32</sup>. Furthermore, PGC-1 $\alpha$  expression was detected in a high percentage of CTCs of metastatic breast cancer patients. Our studies provide insight into uncovered dynamic shifts in the metabolic program of cancer cells to facilitate diverse steps associated with cancer progression and metastasis. □

## METHODS

Methods and any associated references are available in the [online version of the paper](#).

Note: Supplementary Information is available in the [online version of the paper](#)

## ACKNOWLEDGEMENTS

This study was primarily supported by funds from the Cancer Prevention and Research Institute of Texas and funds from MD Anderson Cancer Center (MDACC). J.T.O.C. was financially supported by the DoD Breast Cancer Research Predoctoral Traineeship Award (W81XWH-09-1-0008). R.K. is supported by NIH Grants CA125550, CA155370, CA151925, DK081576 and DK055001. Mass spectrometry work was partially supported by CA12096405 (J.M.A.) and CA00651646 (J.M.A.). We wish to thank B. Spiegelman and J. Estall (Dana Farber Cancer Institute, Boston, Massachusetts, USA) for providing us with reagents related to PGC-1 $\alpha$ . We thank M. Protopopova (MDACC, Houston, Texas) and F. Muller (MDACC, Houston, Texas) for their help with the Seahorse experiments. We thank L. Cantley (BIDMC, Boston, Massachusetts) for his critical reading of the manuscript. We also thank M. Yuan and S. Breitkopf (BIDMC, Boston, Massachusetts) for their help with mass spectrometry experiments, and G. Buruzula and J. LaVecchio at the Joslin Flow Cytometry Core Facility (Joslin Diabetes Center, Boston, Massachusetts) for helping with flow cytometry experiments. For electron microscopy imaging, the High Resolution Electron Microscopy Facility at UTMDACC is supported by the Institutional Core Grant CA16672. We thank R. Langley for help in editing of the manuscript.

## AUTHOR CONTRIBUTIONS

J.T.O.C. performed data analyses and helped with the preparation of figures; K.N.G.H. performed experiments; H.W., K.P. and M.C.H. helped with data analyses; F.M.d.C., L.T.D.C., R.M.R. and J.M.A. performed experiments and analysed data, A.D. performed statistical analyses, V.S.L. performed experiments, analysed the data and contributed to the design of the experiment, writing of the manuscript and preparation of figures, R.K. contributed to the conceptual design of the study and provided advice regarding experiments and writing of the manuscript.

## COMPETING FINANCIAL INTERESTS

The authors declare no competing financial interests.

Published online at [www.nature.com/doi/10.1038/ncb3039](http://www.nature.com/doi/10.1038/ncb3039)

Reprints and permissions information is available online at [www.nature.com/reprints](http://www.nature.com/reprints)

- Warburg, O. On the origin of cancer cells. *Science* **123**, 309–314 (1956).
- Vander Heiden, M. G., Cantley, L. C. & Thompson, C. B. Understanding the Warburg effect: the metabolic requirements of cell proliferation. *Science* **324**, 1029–1033 (2009).
- Ward, P. S. & Thompson, C. B. Metabolic reprogramming: a cancer hallmark even Warburg did not anticipate. *Cancer Cell* **21**, 297–308 (2012).
- DeBerardinis, R. J., Lum, J. J., Hatzivassiliou, G. & Thompson, C. B. The biology of cancer: metabolic reprogramming fuels cell growth and proliferation. *Cell Metab.* **7**, 11–20 (2008).
- Locasale, J. W. & Cantley, L. C. Metabolic flux and the regulation of mammalian cell growth. *Cell Metab.* **14**, 443–451 (2011).
- Gatenby, R. A. & Gillies, R. J. Why do cancers have high aerobic glycolysis? *Nat. Rev. Cancer* **4**, 891–899 (2004).
- Aslakson, C. J. & Miller, F. R. Selective events in the metastatic process defined by analysis of the sequential dissemination of subpopulations of a mouse mammary tumor. *Cancer Res.* **52**, 1399–1405 (1992).
- Kalluri, R. & Weinberg, R. A. The basics of epithelial–mesenchymal transition. *J. Clin. Invest.* **119**, 1420–1428 (2009).
- Thiery, J. P. Epithelial–mesenchymal transitions in tumour progression. *Nat. Rev. Cancer* **2**, 442–454 (2002).
- Wu, Z. *et al.* Mechanisms controlling mitochondrial biogenesis and respiration through the thermogenic coactivator PGC-1. *Cell* **98**, 115–124 (1999).
- Puigserver, P. *et al.* A cold-inducible coactivator of nuclear receptors linked to adaptive thermogenesis. *Cell* **92**, 829–839 (1998).
- Girnun, G. D. The diverse role of the PPAR $\gamma$  coactivator 1 family of transcriptional coactivators in cancer. *Semin. Cell Dev. Biol.* **23**, 381–388 (2012).
- Bhalla, K. *et al.* PGC1 $\alpha$  promotes tumor growth by inducing gene expression programs supporting lipogenesis. *Cancer Res.* **71**, 6888–6898 (2011).
- D'Errico, I. *et al.* Peroxisome proliferator-activated receptor- $\gamma$  coactivator 1- $\alpha$  (PGC1 $\alpha$ ) is a metabolic regulator of intestinal epithelial cell fate. *Proc. Natl Acad. Sci. USA* **108**, 6603–6608 (2011).
- Guy, C. T., Cardiff, R. D. & Muller, W. J. Induction of mammary tumors by expression of polyomavirus middle T oncogene: a transgenic mouse model for metastatic disease. *Mol. Cell Biol.* **12**, 954–961 (1992).
- Cooke, V. G. *et al.* Pericyte depletion results in hypoxia-associated epithelial-to-mesenchymal transition and metastasis mediated by met signaling pathway. *Cancer Cell* **21**, 66–81 (2012).
- Rae, J. M., Creighton, C. J., Meck, J. M., Haddad, B. R. & Johnson, M. D. MDA-MB-435 cells are derived from M14 melanoma cells—a loss for breast cancer, but a boon for melanoma research. *Breast Cancer Res. Treat.* **104**, 13–19 (2007).
- Yuan, M., Breitkopf, S. B., Yang, X. & Asara, J. M. A positive/negative ion-switching, targeted mass spectrometry-based metabolomics platform for bodily fluids, cells, and fresh and fixed tissue. *Nat. Protoc.* **7**, 872–881 (2012).
- Schreiber, S. N., Knutti, D., Brogli, K., Uhlmann, T. & Kralli, A. The transcriptional coactivator PGC-1 regulates the expression and activity of the orphan nuclear receptor estrogen-related receptor  $\alpha$  (ERR $\alpha$ ). *J. Biol. Chem.* **278**, 9013–9018 (2003).
- Woelfle, U. *et al.* Molecular signature associated with bone marrow micrometastasis in human breast cancer. *Cancer Res.* **63**, 5679–5684 (2003).
- Jose, C., Bellance, N. & Rossignol, R. Choosing between glycolysis and oxidative phosphorylation: a tumor's dilemma? *Biochim. Biophys. Acta* **1807**, 552–561 (2011).
- Koppenol, W. H., Bounds, P. L. & Dang, C. V. Otto Warburg's contributions to current concepts of cancer metabolism. *Nat. Rev. Cancer* **11**, 325–337 (2011).
- Hu, J. *et al.* Antitumor therapy provokes ALT and mitochondrial adaptive mechanisms in cancer. *Cell* **148**, 651–663 (2012).
- St-Pierre, J. *et al.* Suppression of reactive oxygen species and neurodegeneration by the PGC-1 transcriptional coactivators. *Cell* **127**, 397–408 (2006).
- Lin, M. T. & Beal, M. F. Mitochondrial dysfunction and oxidative stress in neurodegenerative diseases. *Nature* **443**, 787–795 (2006).
- Yang, M. H. *et al.* Direct regulation of TWIST by HIF-1 $\alpha$  promotes metastasis. *Nat. Cell Biol.* **10**, 295–305 (2008).
- Yu, M. *et al.* Circulating breast tumor cells exhibit dynamic changes in epithelial and mesenchymal composition. *Science* **339**, 580–584 (2013).
- Jones, A. W., Yao, Z., Vicencio, J. M., Karkucinska-Wieckowska, A. & Szabadkai, G. PGC-1 family coactivators and cell fate: roles in cancer, neurodegeneration, cardiovascular disease and retrograde mitochondria-nucleus signalling. *Mitochondrion* **12**, 86–99 (2012).
- Gibbins, J. R. Epithelial cell motility: the effect of 2-deoxyglucose on cell migration, ATP production, and the structure of the cytoplasmic ground substance in lamellipodia of epithelial cells in culture. *Cell Motil.* **2**, 25–46 (1982).
- Schafer, Z. T. *et al.* Antioxidant and oncogene rescue of metabolic defects caused by loss of matrix attachment. *Nature* **461**, 109–113 (2009).
- Schumacher, D., Strilic, B., Sivaraj, K. K., Wettschureck, N. & Offermanns, S. Platelet-derived nucleotides promote tumor-cell transendothelial migration and metastasis via P2Y2 receptor. *Cancer Cell* **24**, 130–137 (2013).
- Suzuki, T. *et al.* Estrogen-related receptor  $\alpha$  in human breast carcinoma as a potent prognostic factor. *Cancer Res.* **64**, 4670–4676 (2004).

## METHODS

**Animal studies.** Orthotopic (mammary fat pad for 4T1 and MDA-MB-231, under the renal capsule for 786-0, and subcutaneous for B16F10 and MDA-MB-235; ref. 17) and intravenous injections of cancer cells were performed as previously described<sup>16,33</sup>. MMTV-PyMT mice were previously described<sup>15</sup> and emergence of primary and secondary tumours in these mice and the experimental endpoint at which PCCs, MCCs and CCCs were assayed were previously described<sup>16</sup>. Adult (at least 8 weeks of age) BALB/c female mice were used for 4T1 injections, adult C57BL/6 male or female mice were used for B16F10 injections, and adult female and male Nu/Nu mice were used for MDA-MB-231, 786-0 and MDA-MB-235 injections.  $n = 5-7$  mice were used per experimental group. The metastatic surface area was computed as previously described<sup>16</sup>. No statistical method was used to predetermine sample size and the experiments were not randomized. The investigators were not blinded to allocation during experiments and outcome assessment. The blood volume taken to collect CCCs was 200  $\mu$ l. Blood was incubated with ACK lysis buffer (2 ml per 200  $\mu$ l of blood for 15 min at 4 °C) before FACS purification based on GFP expression. For CCC colony formation, 200  $\mu$ l of blood treated with ACK lysis buffer was plated in 10 cm<sup>2</sup> dishes in DMEM tissue culture media supplemented with 10% FBS and penicillin/streptomycin. All animal experiments were reviewed and approved by the Institutional Care and Use Committee at the Beth Israel Deaconess Medical Center and University of Texas MD Anderson Cancer Center.

**Cell lines, stable transfection of PGC-1 $\alpha$  shRNA, and overexpression of PGC-1 $\alpha$ .** 4T1 (mouse mammary adenocarcinoma), B16F10 (mouse melanoma), MDA-MB-231 (human mammary adenocarcinoma) and MDA-MB-435 (human melanoma) cell lines were obtained from ATCC and cultured in recommended tissue culture media. Partial gene mutations reported for these lines are listed below (WT: wild-type: no mutation; \* known mutations): 4T1 (P53\*; ref. 7), B16F10 (P53<sup>WT</sup>/Kras<sup>WT</sup>/cMyc<sup>WT</sup>; ref. 34) and MDA-MB-231 (P53\*/Kras\*/cMyc\*; ref. 35). For stable transfection of PGC-1 $\alpha$ , pre-designed shRNAs from Origene were used and puromycin-resistant clones were subsequently propagated. For overexpression of PGC-1 $\alpha$ , recombinant adenovirus expressing PGC-1 $\alpha$  or empty pcDNA control vector was provided by B. Spiegelman (Dana-Farber Cancer Institute, Boston, Massachusetts). For the proliferation rate, cells growing exponentially were counted twice at 12 h intervals and the respective proliferation rate was calculated. Hypoxia experiments were performed as previously described, and re-oxygenation included a 24 h incubation in normoxia (21% oxygen) following a 48 h exposure to hypoxia (1–2% oxygen).

**Gene expression array and real-time PCR validation.** RNA was extracted from PCCs, MCCs and CCCs using RNeasy Plus Mini Kit (Qiagen) and submitted to the Molecular Genetics Core Facility at the Children's Hospital. Microarray analysis was performed using Mouse Ref8 Gene Expression BeadChip (Illumina platform) and Metacore (GeneGo) and Knowledge Based Pathway (IPA; rank invariant normalization with subtracted background). Gene expression validation by real-time PCR was performed as previously described<sup>16</sup> using the primers listed in Supplementary Table 5. Heat maps were drawn using R software. For PGC-1 $\alpha$  expression in the laser-microdissected cancer cells from human invasive ductal carcinoma (IDC) tumour specimens, the SuperScript III One-Step RT PCR System from Invitrogen was used.

**Relative mitochondrial DNA content measurements.** Mitochondrial DNA (mtDNA) was measured by PCR analysis of total DNA extracted from mouse and human CCCs by assessing the relative levels of cytochrome oxidase 1 (mouse mtCO1: 5'-TTGGTCCCCTCCTCCAGC-3' and 5'-CCAGTGCTAGCCG CAGGCA-3') versus  $\beta$ -actin (Supplementary Table 5) and Arp/36b4 (5'-GGAGCC AGCGAGGCCACACTGCTG-3' and 5'-CTGGCCACGTTGCGGACACCTCC-3') and human mtCO1 (5'-TGGAGCCTCCGTAGACCTAA-3' and 5'-TGCGAA GCCTGGTAGGATAA-3') versus  $\beta$ -globin (Supplementary Table 5). For mitochondria protein content, mitochondria were isolated as previously described<sup>36</sup>, with the following modifications: cells plated in 10 cm<sup>2</sup> tissue culture dishes were counted and pelleted at 450g for 5 min at room temperature. The cell pellet was re-suspended in 2 ml of mitochondria isolation medium (MIM) with BSA (MIM: 300 mM sucrose, 10 mM Na-HEPES, 0.2 mM EDTA, pH 7.2; 1 mg ml<sup>-1</sup> BSA) and dounced homogenized. Lysates were spun at 450g for 10 min at 4 °C. The supernatant was then transferred to new tubes and spun at 15,800g for 15 min at 4 °C. The mitochondria pellet was then washed once with 1 ml MIM+BSA and 1 ml MIM. The final pellet was re-suspended in 20  $\mu$ l MIM. A 1:100 dilution of 20  $\mu$ l MIM resuspension was used with the microBCA assay kit (PierceNet) following the manufacturer's directions. Protein content was normalized to cell count.

**Measurement of oxygen consumption rate.** The oxygen consumption rates (OCRs) were measured using the Seahorse XF24 and XF96 instruments (Seahorse Bioscience) under standard conditions and after the addition of 0.1  $\mu$ M oligomycin,

0.05  $\mu$ M FCCP, 1  $\mu$ M rotenone and 10  $\mu$ M atpenin A5. Real-time measurements (triplicates) of the OCR in picomoles per minute in tissue culture medium above cells plated in a microplate were plotted over time before the addition of rotenone to the culture media (basal OCR), and after addition of rotenone to specifically measure mitochondrial respiration. The difference in OCR before and after rotenone addition to the culture media reflects the oxygen consumption by mitochondria (mitochondrial OCR). The OCR measurements were adjusted to cell numbers plated. To this end, the cells were stained with crystal violet (0.1% weight per volume of water) following paraformaldehyde (PFA) permeabilization (4% PFA) and spectrophotometric measurements of 10% acetic-acid-solubilized cells were performed with a standard plate reader (Molecular Devices). For OCR measurements of permeabilized cells, the Seahorse plasma membrane permeabilizer kit was used, allowing cells to permeabilize for 30 min, with media supplemented with 10 mM malate and 10 mM glutamate, and with sequential injection of 4 mM ADP, 2  $\mu$ M rotenone, 10 mM succinate and 2.5  $\mu$ M antimycin A.

**ATP measurements.** ATP measurements were obtained using the ATP Determination kit (Life Technologies). For the latter, cells were homogenized in lysis buffer (1% Triton X-100, 0.1% SDS, 150 mM NaCl, 50 mM Tris-HCl pH 7.5, 1% NaDOC) supplemented with protease cocktail inhibitor, Complete (Roche) and phenylmethylsulphonyl fluoride (Sigma-Aldrich). Protein was quantified by using the BCA Protein Assay (Thermo Scientific), which was used for normalization. Measurements were obtained using the fluorescence plate reader FLUOstar Omega (BMG Labtech). The samples were normalized to the protein concentration of the corresponding Scrbl shRNA cell line.

**Transmission electron microscopy.** Transmission electron microscopy imaging was performed at the High Resolution Electron Microscopy Facility at UTMDACC. Samples fixed with a solution containing 3% glutaraldehyde plus 2% paraformaldehyde in 0.1 M cacodylate buffer, pH 7.3, were washed in 0.1 M cacodylate buffer and treated with 0.1% Millipore-filtered buffered tannic acid, postfixed with 1% buffered osmium tetroxide for 30 min, and stained *en bloc* with 1% Millipore-filtered uranyl acetate. The samples were washed several times in water, then dehydrated in increasing concentrations of ethanol, infiltrated, and embedded in LX-112 medium. The samples were polymerized in a 60 °C oven for about 2 days. Ultrathin sections were cut in a Leica Ultracut microtome (Leica), stained with uranyl acetate and lead citrate in a Leica EM Stainer, and examined in a JEM 1010 transmission electron microscope (JEOL) at an accelerating voltage of 80 kV. Digital images were obtained using the AMT Imaging System (Advanced Microscopy Techniques). For quantification, we examined 3–9 cells magnified at  $\times 5,000$  per group and counted the number of mitochondria per cell visualized in the sectioned image.

**Targeted mass spectrometry analysis.** For cultured cells as well as FACS-purified cells, 4 ml or 400 ml of 80% LC-MS-grade methanol was added to each 10 cm<sup>2</sup> dish or FACS sample respectively and incubated at –80 °C for 15 min. Cells were scraped off the dish using a sterile cell scraper and collected from the plate to be centrifuged at 18,470g for 5 min in a cold room to pellet cell debris and proteins. Supernatants were saved. Pellets were resuspended in 500  $\mu$ l 80% methanol by vortexing and subsequently centrifuged as before. Supernatants were centrifuged one final time at 18,470g for 10 min at 4 °C. Metabolite extractions were dried to a pellet by SpeedVac with no heat. Samples were re-suspended using 20  $\mu$ l LC-MS-grade water and 10  $\mu$ l was injected and analysed using a 5500 QTRAP hybrid triple quadrupole mass spectrometer (AB/Sciex) coupled to a Prominence UFLC HPLC system (Shimadzu) through selected reaction monitoring (SRM). Two hundred and fifty-four endogenous water-soluble metabolites were targeted for steady-state analyses of samples. Some metabolites were targeted in both the positive and negative ion mode through positive/negative polarity switching for a total of 289 SRM transitions. The ESI voltage was +4900 V in the positive ion mode and –4500 V in the negative ion mode. The dwell time was 3 ms per SRM transition and the total cycle time was  $\sim 1.56$  s. Approximately 10–12 data points were acquired per detected metabolite. Samples were delivered to the MS through normal-phase chromatography using a 4.6 mm i.d.  $\times$  10 cm Amide XBridge HILIC column (Waters) at 350  $\mu$ l min<sup>-1</sup>. Gradients were run starting from 85% buffer B (HPLC grade acetonitrile) to 35% B from 0–3.5 min; 35% B to 2% B from 3.5–11.5 min; 2% B was held from 11.5–16.5 min; 2% B to 85% B from 16.5–17.5 min; 85% B was held for 7 min to re-equilibrate the column. Buffer A was comprised of 20 mM ammonium hydroxide/20 mM ammonium acetate (pH 9.0) in 95:5 water/acetonitrile. Peak areas from the total ion current for each metabolite SRM transition were integrated using MultiQuant v2.0 software (AB/Sciex). Metabolomics data analysis was done in part using Metaboanalyst software ([www.metaboanalyst.ca](http://www.metaboanalyst.ca)). For glucose isotopic tracer experiments, cells were placed in glucose-free media supplemented with 10% dialysed serum and with uniformly labelled [<sup>13</sup>C<sub>6</sub>] glucose (Cambridge Isotope Laboratories) for 12 h before extraction for LC-MS/MS analyses. A set of SRM transitions was used to target the heavy form of each metabolite.

**Invasion and migration assays.** For invasion assays, the polycarbonate membranes (8 µm pore) were coated on both sides with Matrigel and cells on the basal side of the membrane (post migration) were fixed in 100% ethanol and stained with haematoxylin before microscopic evaluation. For the scratch/migration assay, the cell-free area was measured 24 h after scratching the dish, and 0.1 µM rotenone was used.

**Anoikis assay.** Cells ( $5 \times 10^6$ ) were serum-starved in 0.5% FBS for 24 h. The cells were then counted and resuspended in 13 ml serum-free DMEM in a 15 ml Falcon tube and allowed to rock at 37 °C for 24 h. The cells were then pelleted and counted using a haemocytometer. Triplicate measurements of two cell counts were used to determine the percentage of cell viability.

**Type I collagen contractility assay.** Cells were seeded at a density of  $5 \times 10^4$  cells per well of 24-well plates on 3 mg ml<sup>-1</sup> type I collagen gel. Stressed matrix was allowed to contract for 48 h and was then released. Collagen gel size change (average gel area) was measured with a ruler 24 h following release of stressed matrix.

**FACS.** Tumours were resected, minced, and digested in 400 U ml<sup>-1</sup> type II collagenase at 37 °C while shaking. Single-cell suspensions following filtering through 75 µm mesh were fixed in BD Cytotfix/Cytoperm (BD Biosciences) and stained in 2% FBS containing PBS with DMEM with anti-mouse αSMA primary antibody and TRITC-conjugated secondary antibody. All FACS analyses were performed at the Joslin Diabetes Center Flow Cytometry Core. FACS-purified cells were spun down at 2,000g for 10 min at 25 °C and the cell pellet was processed for quantitative PCR analysis using the Cells-to-cDNA kit (Ambion) according to the manufacturer's directions. CCCs and PCCs were also FACS-purified and cytospin (onto glass slides at 130g for 5 min) stained following a 10 min acetone fixation step at 4 °C.

**Immunostaining.** Thin frozen sections (5 µm) were immunolabelled and quantification of immunolabelling was performed as previously described<sup>16</sup>. Antibody-related information for stainings on mouse tissues and cells: PGC-1α (1:200; clone 4C1.3, Calbiochem ST1202), Twist (1:200; Santa Cruz Biotechnology, H-81), CK8 (1:200; DSHB TROMA-1) and αSMA (1:200; clone 1A4, Sigma-Aldrich F3777).

**Western blot analyses.** Western blot analyses were performed as previously described<sup>16</sup>, using anti-PGC-1α antibody (1 µg ml<sup>-1</sup>; clone 4C1.3, Calbiochem ST1202) as recommended by the manufacturer. In Fig. 3b, the results were obtained with samples from the same experiment and on two separate blots that were processed in parallel.

**Patient information and data collection.** For the data presented in Fig. 8a, patients were diagnosed with breast cancer and tumours were surgically resected at the Department of Gynecology, University Medical Center Hamburg-Eppendorf. Written informed consent was obtained and the study was approved by the University Medical Center Hamburg-Eppendorf institutional review board. Material collection and processing were previously described<sup>37</sup> and RNA was characterized from patients diagnosed with IDC (all early-stage oestrogen-receptor-responsive primary tumours) with known bone marrow aspirate positivity status. Detection of disseminated tumour cells in bone marrow was performed with anti-cytokeratin monoclonal antibody A45-B/B3 as previously described<sup>38</sup> and according to international standards<sup>39</sup>. Patient information details are provided in Supplementary Table 1. For the data presented in Fig. 8b–d, 161 de-identified samples were collected from patients with IDC recruited for biopsy at the A. C. Carmargo Hospital, after informed consent from patients and approval by the institutional review board. The tissue microarrays were constructed from 1.50 mm cores of formalin-fixed paraffin-embedded breast tissue. Immunohistochemistry was performed using the anti-PGC-1α antibody (Calbiochem ST1202, clone 4C1.3, 1 µg ml<sup>-1</sup>) as recommended by the manufacturer. Immunohistochemistry evaluation was performed by selecting invasive cancer cells, as defined by isolated cells, the smallest isolated nests of cells, cells from the border of solid tumours, and cells that were invading adipose tissue, stroma or micro emboli. The staining intensity for PGC-1α in these cells was automatically measured using the APERIO system. A Martingale residual plot was used for assessing a threshold for PGC-1α, and this threshold was used for

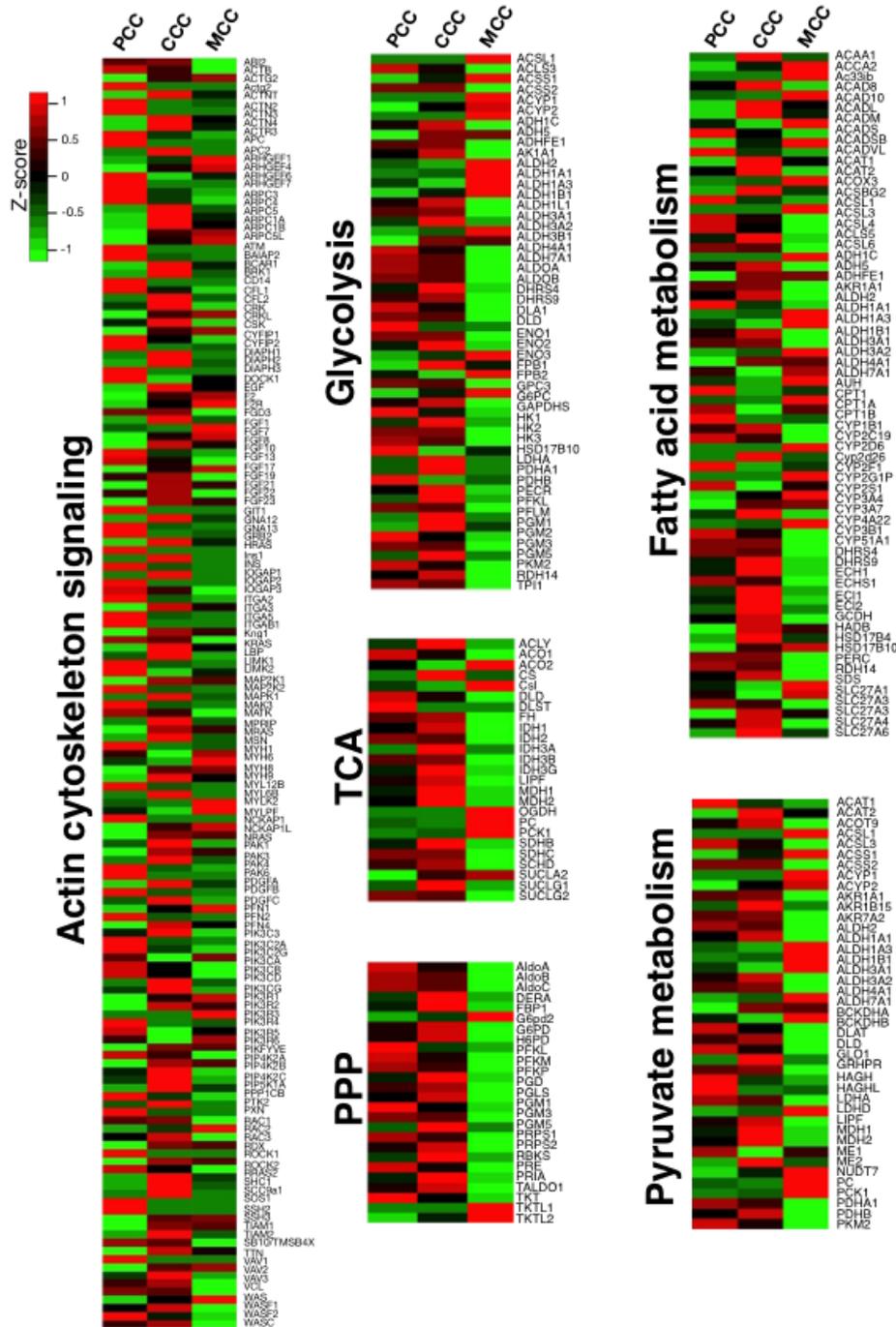
correlative analyses with clinical variables (Supplementary Table 2 and Fig. 8d) and survival (Fig. 8c). In Fig. 8c, clinical information was missing for 3 patients to define disease-free survival. The observers were blinded when performing these analyses. For the data presented in Fig. 8e, four patients (Supplementary Table 3) were recruited for CCC enrichment at the A. C. Carmargo Hospital, after patient informed consent and approval by the institutional review board were obtained. Patient peripheral blood sample (8 ml) was collected into an EDTA tube and diluted 1:10 with ISET buffer (RareCell Diagnostics)<sup>40</sup>. An additional 13 IDC patients with lung metastasis were recruited for CTC evaluation as described above (Supplementary Table 4). After 10 min at room temperature the sample was loaded into a well of ISET Block (RareCell Diagnostics), with 8-µm-diameter cylindrical pores, above a polycarbonate membrane. The blood sample was filtered by aspiration under vacuum of -10 kPa and then the membrane was washed by aspiration with PBS buffer. The membrane was disassembled from the ISET Block, allowed to air-dry and stored at -20 °C. The ISET membranes were then hydrated with 70 µl of Tris-saline buffer (TBS) for 10 min followed by vertical draining on absorbent paper towel. In a moist chamber, the cells were permeabilized with 70 µl of TBS 0.2% Triton X-100, for 5 min at room temperature. The membranes were rinsed with TBS, incubated for 15 min in the dark at room temperature with 3% hydrogen peroxide solution, and rinsed again with TBS. The membranes were then stained using antibodies against CK8 (1:50; clone NCL-L-CK8-TS1, Novocastra), PGC-1α (1:200; clone 4C1.3, Calbiochem) or CD45 (clone 2B11 + PD7/26, Dako). For negative controls, primary antibodies were omitted. The primary antibodies were allowed to incubate for 1 h at room temperature. The membranes were then rinsed with TBS and developed using the Dual long system HRP (Dako; 30 min, room temperature) and DAB chromogen (Dako) and Permanent red (Dako; 5 min, room temperature). The membranes were then rinsed with deionized water twice and counterstained with Harris's haematoxylin for 1 min. On average 1.73 CTCs in 1 ml of blood were analysed.

**Statistical analyses.** Significance was determined by one-way ANOVA or unpaired two-tailed Student's *t*-test and *P* < 0.05 was considered statistically significant. Correlative analysis for PGC-1α transcript levels in cancer cells laser-microdissected from breast tumours of IDC patients (the median dCt was used as the cut-off to define 'high' and 'low' PGC-1α transcript level) with bone marrow DTC status (positive or negative) employed a one-sided  $\chi^2$  test. Association between clinical characteristics and PGC-1α expression levels was verified by a two-tailed Fisher's exact test. For survival analysis, Kaplan–Meier curves were drawn and differences between the curves were calculated by the log-rank test<sup>41</sup> using R Foundation for Statistical Computing (2010) software. \**P* < 0.05 was considered statistically significant. Analysis of microarray data was performed using Metacore (GeneGo) and Knowledge Based Pathway (IPA; *P* < 0.05).

**Gene expression array accession number.** The gene expression array data were deposited in the Gene Expression Omnibus database (accession number GSE37344).

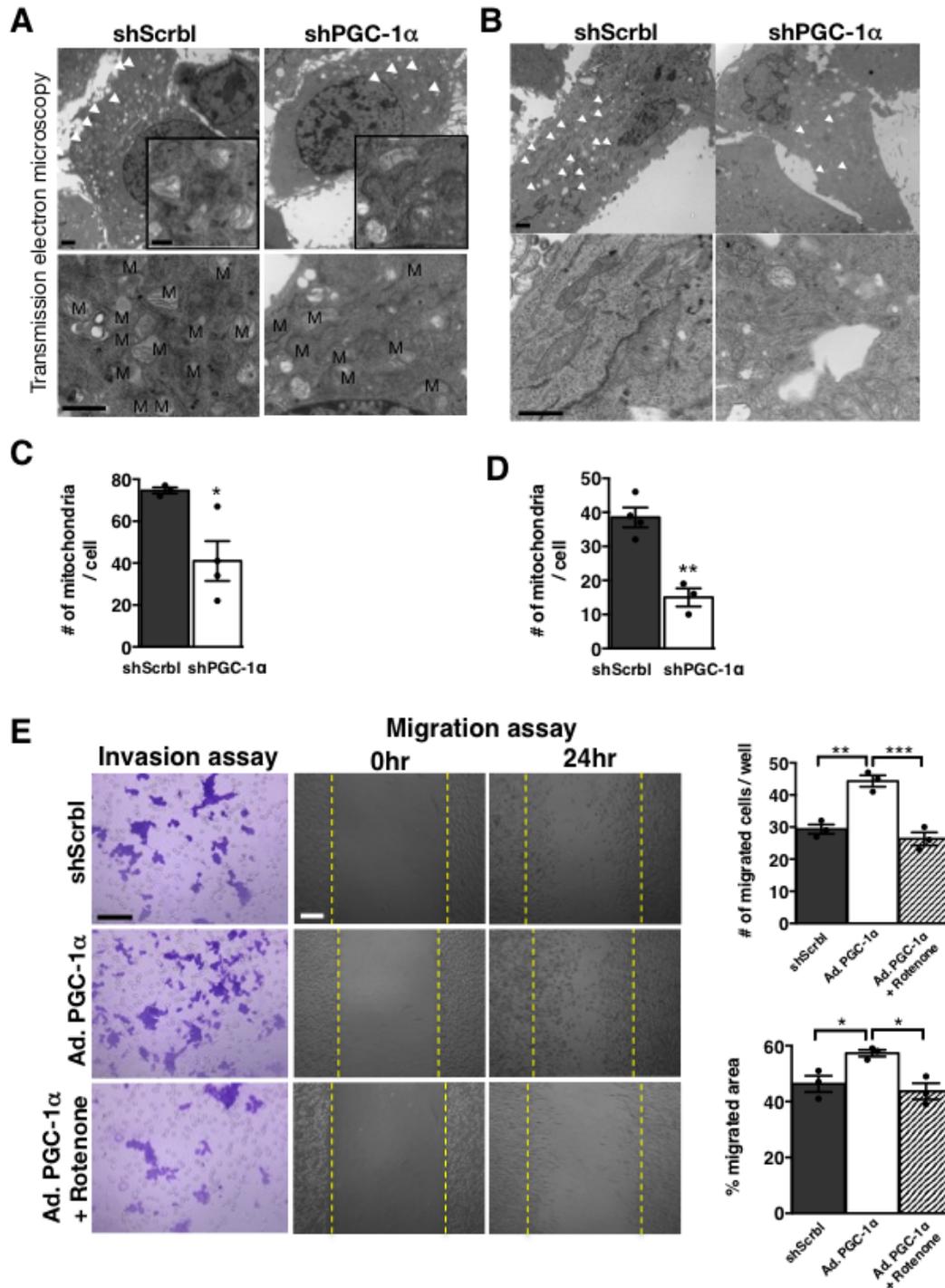
33. O'Connell, J. T. *et al.* VEGF-A and Tenascin-C produced by S100A4+ stromal cells are important for metastatic colonization. *Proc. Natl Acad. Sci. USA* **108**, 16002–16007 (2011).
34. Castle, J. C. *et al.* Exploiting the mutanome for tumor vaccination. *Cancer Res.* **72**, 1081–1091 (2012).
35. Barretina, J. *et al.* The Cancer Cell Line Encyclopedia enables predictive modelling of anticancer drug sensitivity. *Nature* **483**, 603–607 (2012).
36. Boehm, E. A., Jones, B. E., Radda, G. K., Veech, R. L. & Clarke, K. Increased uncoupling proteins and decreased efficiency in palmitate-perfused hyperthyroid rat heart. *Am. J. Physiol. Heart Circ. Physiol.* **280**, H977–H983 (2001).
37. Woelfle, U. *et al.* Molecular signature associated with bone marrow micrometastasis in human breast cancer. *Cancer Res.* **63**, 5679–5684 (2003).
38. Braun, S. *et al.* Cytokeratin-positive cells in the bone marrow and survival of patients with stage I, II, or III breast cancer. *N. Engl. J. Med.* **342**, 525–533 (2000).
39. Fehm, T. *et al.* A concept for the standardized detection of disseminated tumor cells in bone marrow from patients with primary breast cancer and its clinical implementation. *Cancer* **107**, 885–892 (2006).
40. Hofman, V. *et al.* Morphological analysis of circulating tumour cells in patients undergoing surgery for non-small cell lung carcinoma using the isolation by size of epithelial tumour cell (ISET) method. *Cytopathology* **23**, 30–38 (2012).
41. Balakrishnan, N. & Rao, C. R. *Handbook of Statistics* 1st edn, Vol. 23 (North Holland, 2004).

DOI: 10.1038/ncb3039



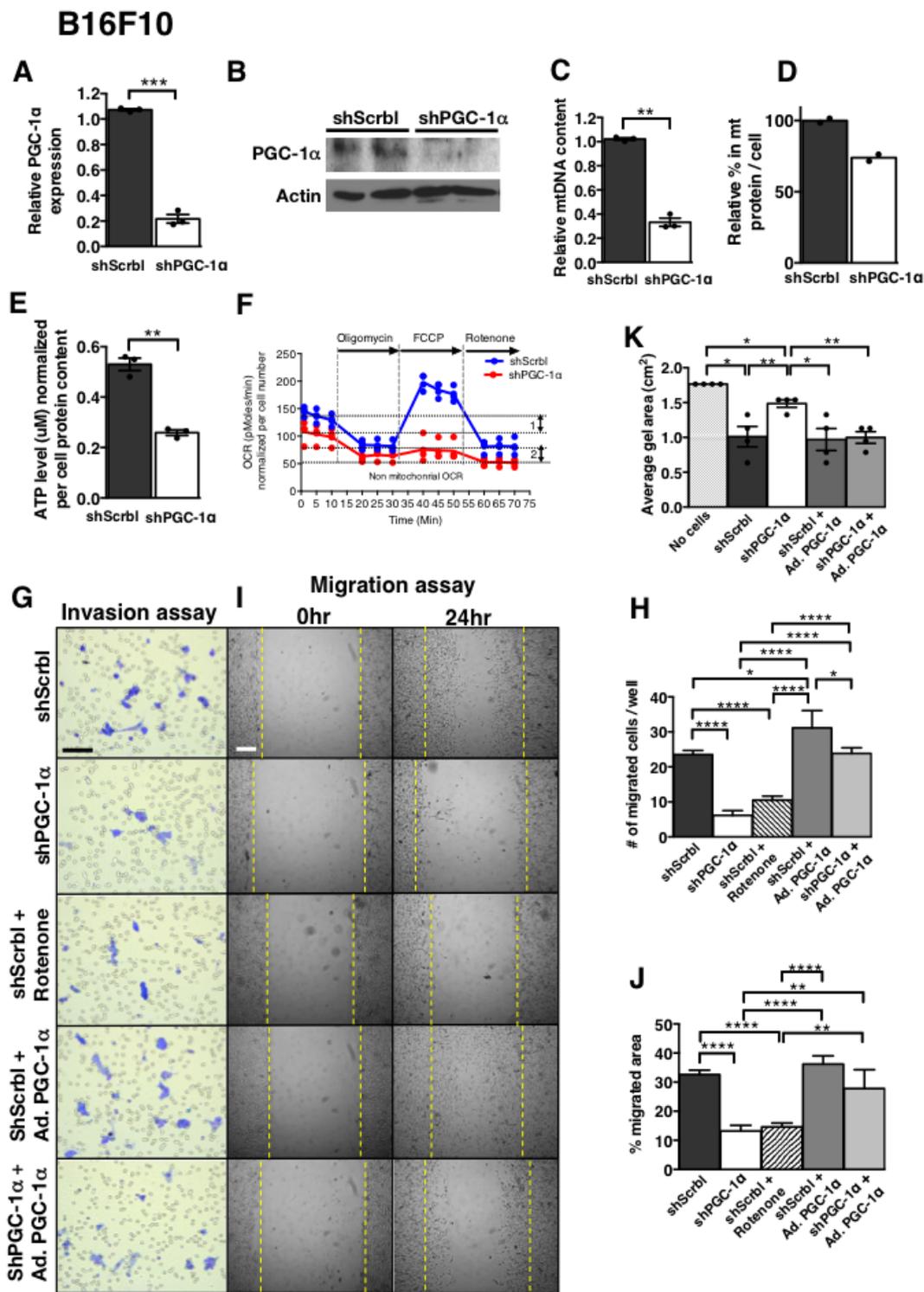
**Supplementary Figure 1** Microarray heat maps of differentially regulated genes. Heat maps rendering of the indicated metabolism pathways in PCC, CCC and MCC.





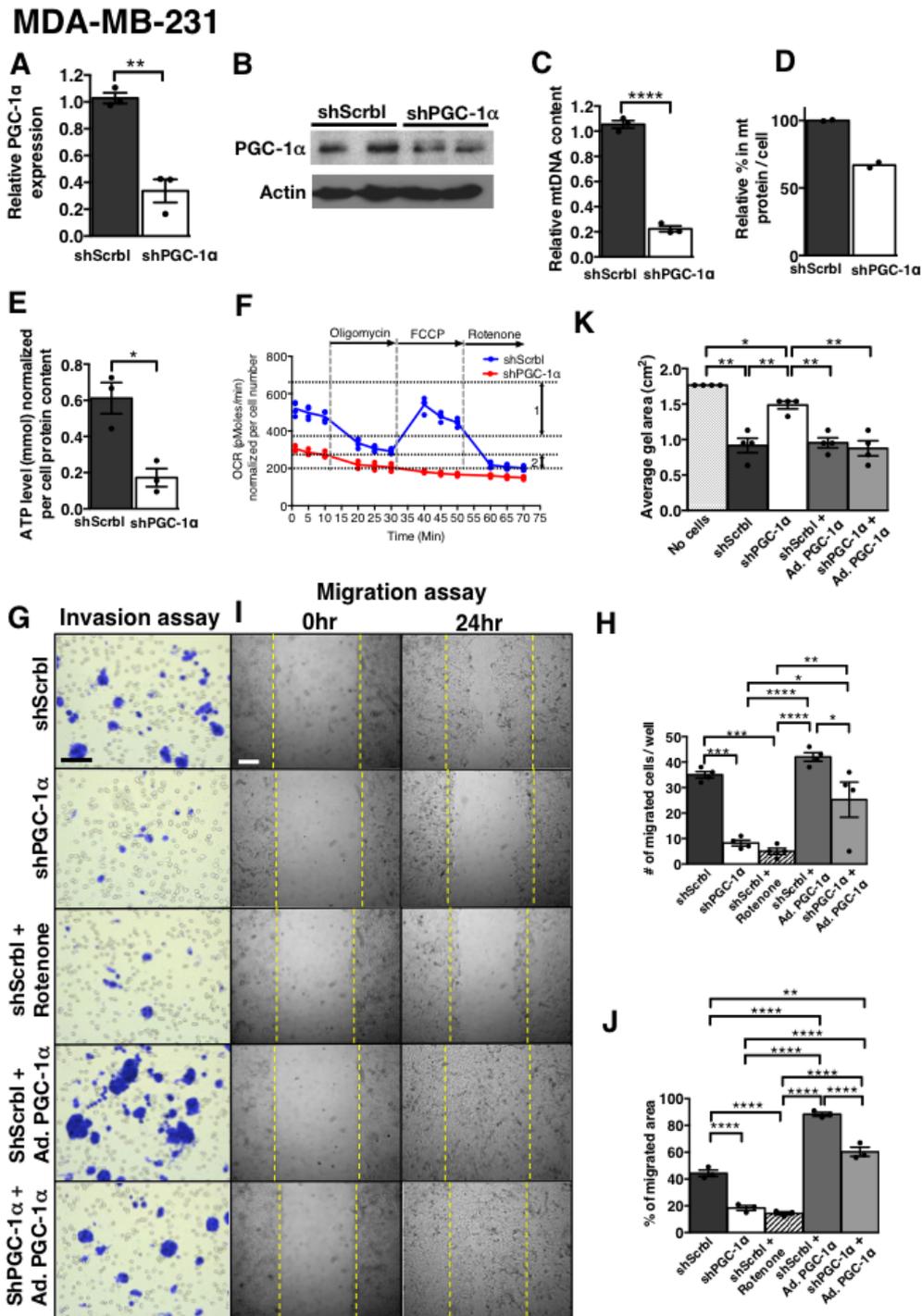
**Supplementary Figure 3** PGC-1 $\alpha$  knockdown is associated with decreased mitochondria number and impairs invasion and migration of cancer cells in a complex I dependent manner. **A-B.** Transmission electron microscopy images of MDAMB231 shScrbl and shPGC-1 $\alpha$  cells (A) and B16F10 shScrbl and shPG1 $\alpha$ , (B) white arrowheads and 'M' identify mitochondria. Scale bar upper panel: 2 mm, insert and lower panel: 500 nm. **C-D.** Quantification of the number of mitochondria per cell in MDAMB231 (shScrbl, n=3 cells; shPGC-1 $\alpha$ , n=4 cells) (C) and B16F10 (shScrbl, n=4

cells; shPGC-1 $\alpha$ , n=3 cells), unpaired two-tailed Student's t-test. Scale bar upper panel: 2 mm, insert and lower panel: 500 nm. **E.** Hematoxylin stained 4T1 cells following invasion, and light microscopy imaging of migrated cells in scratch assay migration, quantitation of invasion assay (n=3 wells/group) and migration assay (n=3 wells/group). Scale bar: 50mm. One-way ANOVA. Ad. PGC-1 $\alpha$ : adenoviral induction of PGC-1 $\alpha$  expression. Data is represented as mean  $\pm$  SEM. \* p<0.05, \*\* p<0.01, \*\*\* p<0.001.



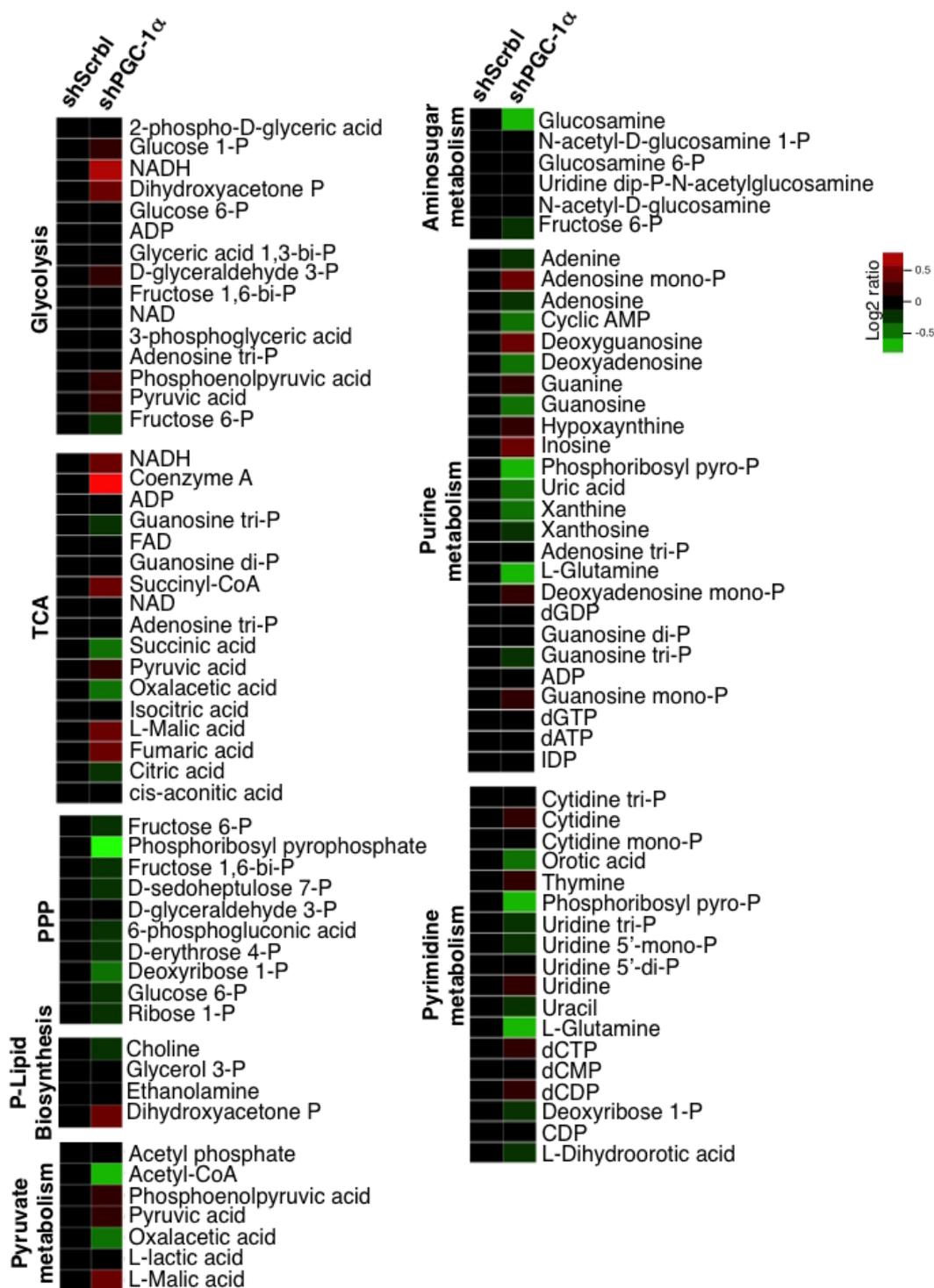
**Supplementary Figure 4** Knockdown of PGC-1α in B16F10 cells suppresses their mitochondria function and invasive properties. **A**. Relative PGC-1α expression in B16F10shPGC-1α cells, normalized to B16F10shScrbl cells (n=3 RNA samples/cell line, unpaired two-tailed Student's t-test). **B**. Western blot for PGC-1α in B16F10shPGC-1α and B16F10shScrbl cells. See also Supplementary Figure 9. **C**. Relative mitochondrial DNA (mtDNA) content (n=3 DNA samples/cell line, unpaired two-tailed Student's t-test) and **D**. mitochondrial protein content (n=2 lysates/cell line) relative to total cell protein content in B16F10shPGC-1α normalized to B16F10shScrbl cells. **E**. Intracellular ATP levels in B16F10shPGC-1α normalized to B16F10shScrbl

cells (n=3 lysates/cell line, unpaired two-tailed Student's t-test). **F**. Oxygen consumption rate (OCR) in B16F10shPGC-1α normalized to B16F10shScrbl cells (n=4 wells/cell line). **G**. Hematoxylin stained B16F10 cells following invasion (scale bar: 50 mm), and **H**. quantitation of invasion assay (n=6 wells/group, one-way ANOVA). Ad. PGC-1α: adenoviral induction of PGC-1α expression. **I**. Light microscopy imaging (scale bar: 50 mm) of migrated cells in scratch assay and **J**. quantitation of migration assay (n=5 wells/group, one-way ANOVA). **K**. Type I collagen gel area reflecting gel contraction by indicated cells (n=4 wells/group, unpaired two-tailed Student's t-test). Data is represented as mean +/- SEM. \* p<0.05, \*\* p<0.01, \*\*\* p<0.001, \*\*\*\* p<0.0001.

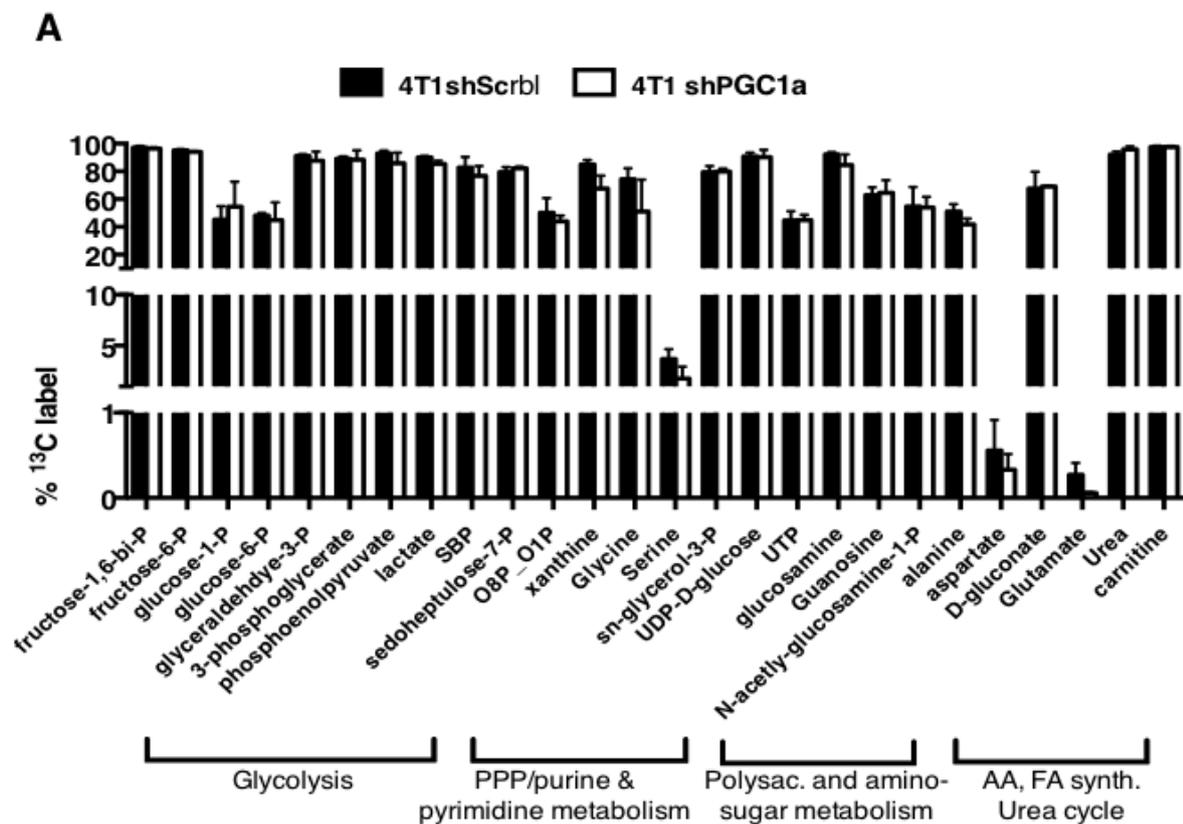


**Supplementary Figure 5** Knockdown of PGC-1 $\alpha$  in MDA-MB-231 cells suppresses their mitochondria function and invasive properties. **A**. Relative PGC-1 $\alpha$  expression in MDA-MB-231shPGC-1 $\alpha$  cells, normalized to MDA-MB-231shScrbl cells (n=3 RNA samples/cell line, unpaired two-tailed Student's t-test). **B**. Western blot for PGC-1 $\alpha$  in MDA-MB-231shPGC-1 $\alpha$  and MDA-MB-231shScrbl cells. See also Supplementary Figure 9 **C**. Relative mitochondrial DNA (mtDNA) (n=3 DNA samples/cell line, unpaired two-tailed Student's t-test) and **D**. mitochondrial protein content relative to total cell protein content (n=2 lysates/cell line) in MDA-MB-231shPGC-1 $\alpha$  normalized to MDA-MB-231shScrbl cells. **E**. Intracellular ATP levels in MDA-MB-231shPGC-1 $\alpha$  normalized to MDA-MB-231shScrbl cells (n=3 lysates/

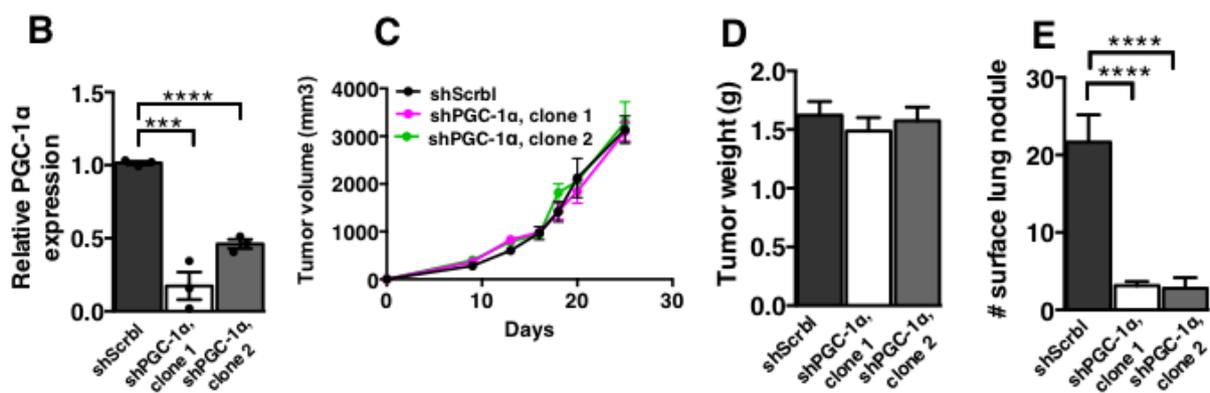
cell line, unpaired two-tailed Student's t-test). **F**. Oxygen consumption rate (OCR) in MDA-MB-231shPGC-1 $\alpha$  (n=3 wells) normalized to MDA-MB-231shScrbl cells (n=4 wells). **G**. Hematoxylin stained MDA-MB-231 cells following invasion (scale bar: 50 mm), and **H**. quantitation of invasion assay (n=4 wells/group, one-way ANOVA). Ad. PGC-1 $\alpha$ : adenoviral induction of PGC-1 $\alpha$  expression. **I**. Light microscopy imaging (scale bar: 50 mm) of migrated cells in scratch assay and **J**. quantitation of migration assay (n=3 wells/group, one-way ANOVA). **K**. Type I collagen gel area reflecting cell contraction by indicated cells (n=4 wells/group, unpaired two-tailed Student's t-test). Data is represented as mean  $\pm$  SEM. \* p<0.05, \*\* p<0.01, \*\*\* p<0.001, \*\*\*\*p < 0.0001. ns: not significant.



**Supplementary Figure 6** Changes in metabolites associated with PGC-1 $\alpha$  suppression. Heat map rendering of the metabolites measured by targeted metabolomics analyses in the indicated metabolism pathways of 4T1sh PGC-1 $\alpha$  normalized to 4T1shScrbl cells (arbitrarily set to 0).

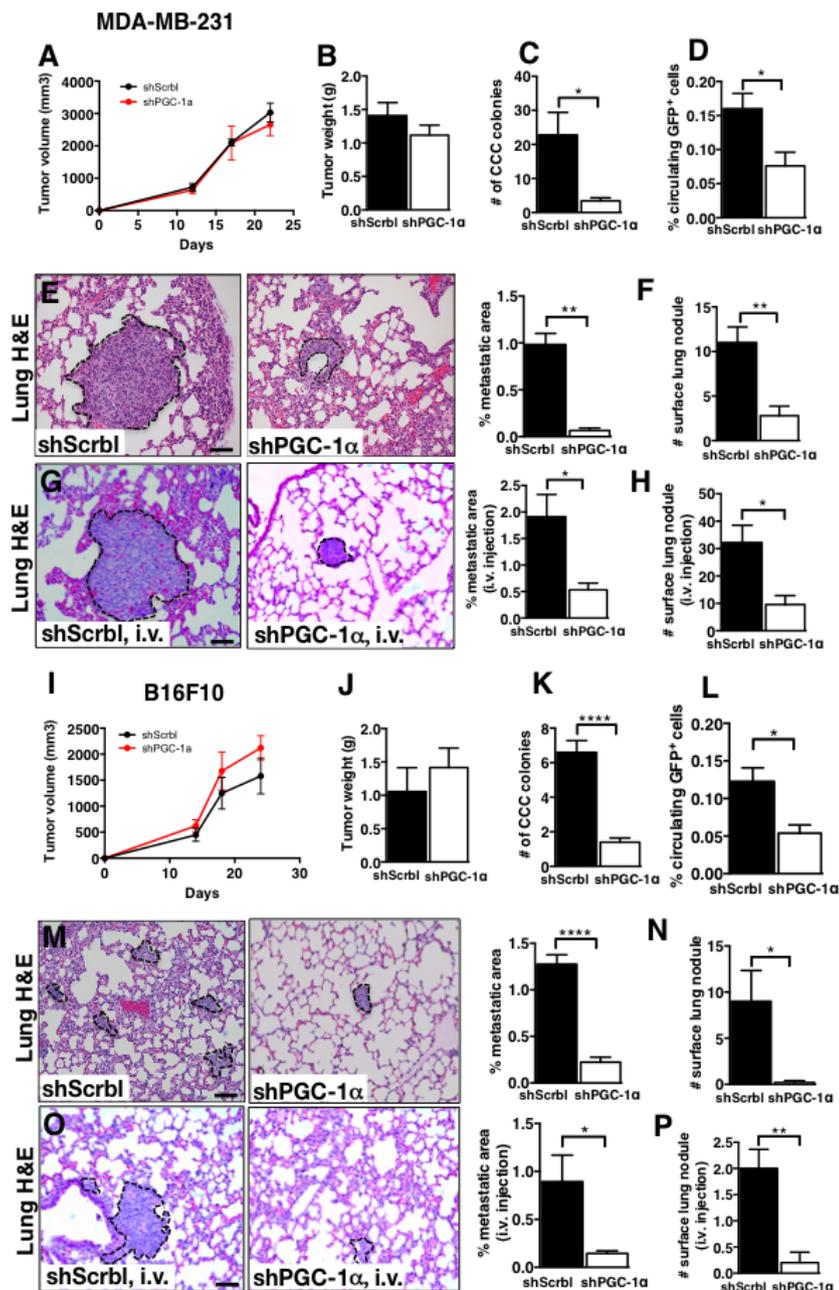


**4T1**



**Supplementary Figure 7** PGC-1 $\alpha$  suppression minimally impact glycolysis but impairs metastasis. A. Percent <sup>13</sup>C labelled metabolites derived from labelled glucose fed to 4T1shPGC-1 $\alpha$  and 4T1shScrbl cells. Metabolites are clustered with respect to the listed metabolic pathways they are associated with. n=3 wells/cell line. PPP, pentose phosphate pathway; Polysac., polysaccharides; AA (amino acids) and FA (fatty acids) synthesis. Statistics source data can be found in Supplementary Table 6. B. Relative PGC-1 $\alpha$  expression in two clones of 4T1shPGC-1 $\alpha$  normalized to 4T1shScrbl cells

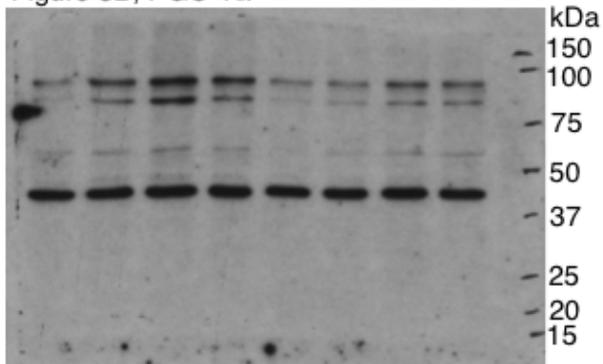
(shScrbl: n=3, shPGC-1 $\alpha$  clone 1: n=3, shPGC-1 $\alpha$  clone 2: n=4 RNA samples/cell line, unpaired two-tailed Student's t-test). C. Tumor volume measured over time and D. Tumor weight at experimental endpoint (shScrbl, n=6 mice; shPGC-1 $\alpha$  clone 1, n=7 mice; shPGC-1 $\alpha$  clone 2, n=5 mice). E. Number of surface lung nodules in 4T1 orthotopic tumor model (shScrbl, n=6 mice; shPGC-1 $\alpha$  clone 1, n=7 mice; shPGC-1 $\alpha$  clone 2, n=5 mice, one-way ANOVA). Data is represented as mean +/- SEM. \*\*\* p < 0.001, \*\*\*\* p < 0.0001.



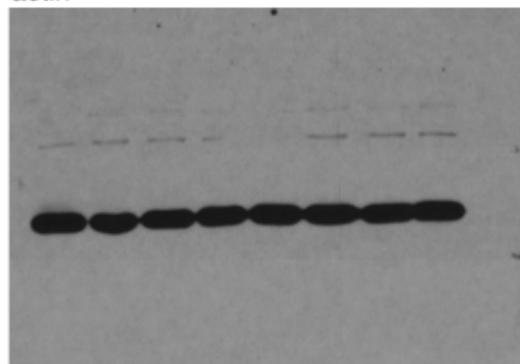
**Supplementary Figure 8** Knockdown of PGC-1 $\alpha$  in MDA-MB-231 and B16F10 cells impairs metastasis. **A**. MDA-MB-231shScrbl and MDA-MB-231shPGC-1 $\alpha$  cells were implanted in the mammary fat pad of nude mice. Tumor volume measured over time. **B**. Tumor weight at experimental endpoint. **C**. Number of CCC colonies formed. **D**. Percent of GFP<sup>+</sup> cancer cells per 200ml blood collected at experimental endpoint. **E**. Representative images of H&E stained lung sections and quantitation of percent metastatic lung surface area relative to total lung surface area. Metastatic lung nodules are circled. Scale bar: 50mm. **F**. Number of lung surface nodules. For **A-F**: MDA-MB-231shScrbl, n=5 mice; MDA-MB-231shPGC-1 $\alpha$ , n=5 mice, unpaired two-tailed Student's t-test. **G**. Representative images of H&E stained lung sections of mice with i.v. injection of indicated cells and percent metastatic surface area relative to total lung surface area. Lung nodules are circled. Scale bar: 50mm. **H**. Number of lung surface nodules following i.v. injection of indicated cells. For **G-H**: MDA-MB-231shScrbl, n=5 mice; MDA-MB-231shPGC-1 $\alpha$ , n=5 mice, unpaired

two-tailed Student's t-test. **I**. B16F10shScrbl and B16F10shPGC-1 $\alpha$  cells were implanted subcutaneously in C57Bl/6 mice. Tumor volume measured over time. **J**. Tumor weight at experimental endpoint. **K**. Number of CCC colonies formed. **L**. Percent of GFP<sup>+</sup> cancer cells per 200ml blood collected at experimental endpoint. **M**. Representative images of H&E stained lung sections and quantitation of percent metastatic lung surface area relative to total lung surface area. Metastatic lung nodules are circled. Scale bar: 50mm. **N**. Number of lung surface nodules. For **I-N**: B16F10shScrbl, n=5 mice; B16F10shPGC-1 $\alpha$ : n=5 mice, unpaired two-tailed Student's t-test. **O**. Representative images of H&E stained lung sections of mice with i.v. injection of indicated cells and percent metastatic surface area relative to total lung surface area. Lung nodules are circled. Scale bar: 50mm. **P**. Number of lung surface nodules following i.v. injection of indicated cells. For **O-P**: B16F10shScrbl, n=5 mice; B16F10shPGC-1 $\alpha$ : n=5 mice, unpaired two-tailed Student's t-test. Data is represented as mean  $\pm$  SEM. \* p<0.05, \*\* p<0.01, \*\*\*\* p<0.0001.

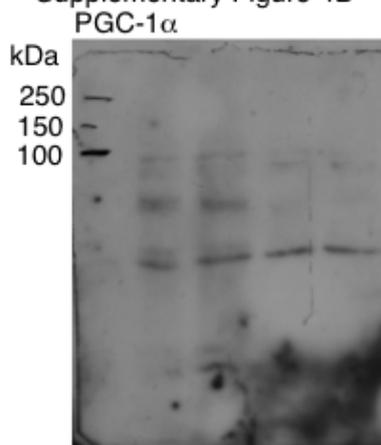
Figure 3B, PGC-1 $\alpha$



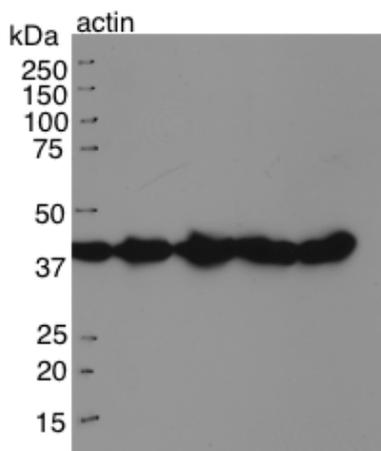
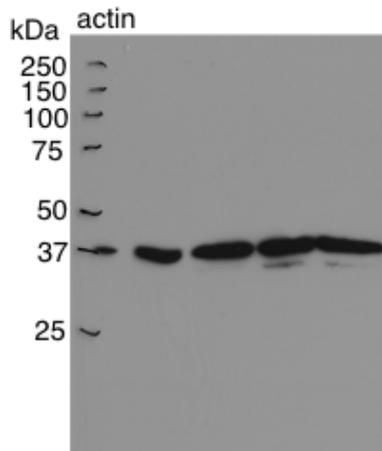
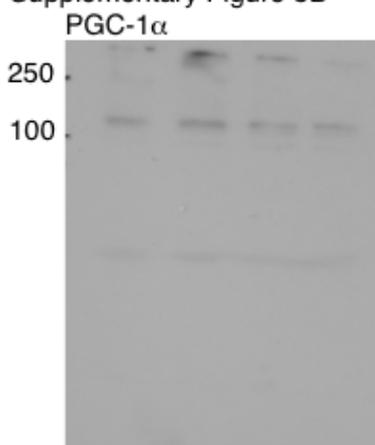
actin



Supplementary Figure 4B



Supplementary Figure 5B



Supplementary Figure 9 Uncropped western blots.

<b>Supplementary Table 1. Patient information related to Figure 8A</b>					
		<b>Primary tumors</b>			
		<b>BM positive</b>		<b>BM negative</b>	
		<b>n</b>	<b>%</b>	<b>n</b>	<b>%</b>
<b>Histology</b>					
	Ductal	12	85.7	16	100.0
	others	2	14.3	0	0.0
<b>Tumor stage</b>					
	pT1	5	35.7	7	43.8
	pT2	9	64.3	9	56.2
	pT3+4				
<b>Lymph node status</b>					
	pN0	12	85.7	16	100.0
	pN positive	2	14.3	0	0.0
<b>Metastatic status</b>					
	M0	14	100.0	16	100.0
	M1	0	0.0	0	0.0
<b>Grade</b>					
	GI	1	7.1	0	0.0
	GII	9	64.3	9	56.3
	GIII	4	28.6	7	43.7
<b>Age</b>					
	<50	3	21.4	5	31.3
	>50	11	78.6	11	68.7
<b>Hormone receptor</b>					
	negative	0	0.0	1	6.3
	positive	14	100.0	15	93.8
<b>HER2 in prim. tum.</b>					
	negative	13	92.9	11	68.8
	positive	1	7.1	5	31.2
<b>Relapse</b>					
	no	12	85.7	16	100.0
	yes	2	14.3	0	0.0

**Supplementary Table 1, Patient information pertaining to Figure 8A.**

Patients with invasive ductal carcinoma of the breast were categorized based on the presence of disseminated tumor cells in the bone marrow (BM positive: DTC detected in the bone marrow, BM: negative DTC detection). The patient demographic and clinical findings summary is listed for each category.

<b>Supplementary Table 2. Patient information related to Figure 8C-D</b>					
		<b>Primary tumors</b>			
		<b>PGC1a &gt; 150.572 (high)</b>		<b>PGC1a &lt; 150.572 (low)</b>	
		<b>n = 104</b>	<b>%</b>	<b>n = 57</b>	<b>%</b>
<b>Tumor size</b>					
	> 2.0cm	6	5.8	5	8.8
	2.0 to 5.0cm	55	52.9	39	68.4
	< 5.0cm	39	37.5	11	19.3
	unknown	4	3.8	2	3.5
<b>Depth of invasion</b>					
	pT1	4	3.8	5	8.8
	pT2	30	28.8	17	29.8
	pT3	1	1.0	0	0.0
	pT4	69	66.3	33	57.9
	pTX	0	0.0	2	3.5
<b>Lymph node status</b>					
	pN0	38	36.5	29	50.9
	pN1	38	36.5	21	36.8
	pN2	28	26.9	7	12.3
<b>Stage</b>					
	I	0	0.0	1	1.8
	IIA	30	28.8	21	36.8
	IIB	4	3.8	1	1.8
	IIIA	3	2.9	0	0.0
	IIIB	67	64.4	34	59.6
	IV	0	0.0	0	0.0
<b>Distant Metastasis</b>					
	Yes	81	77.9	2	3.5
	No	23	22.1	55	96.5

**Supplementary Table 2, Patient information pertaining to Figure 8B-C.**

Patients with invasive ductal carcinoma of the breast were categorized based on the measured expression of PGC-1 $\alpha$  in primary breast tumor as assayed by tissue microarray staining and scoring for PGC-1 $\alpha$  expression (high or low). The clinical finding summary is listed for each group.

**Supplementary Table 3. Patient information related to Figure 8E**

	<b>Age (at blood collection)</b>	<b>Histopathological classification</b>	<b>IHC features</b>	<b>Stage</b>	<b>Metastasis</b>	<b>Treatment</b>
Patient 1	50	IDC	Triple negative	IV	Bone	Chemotherapy
Patient 2	62	IDC	<i>Her-2 overexpressing</i>	IV	Liver	Chemotherapy
Patient 3	38	IDC	<i>Her-2 overexpressing</i>	IV	Bone, Liver, CNS	Immunotherapy
Patient 4	44	IDC	<i>Luminal B</i>	I	Bone, Lung, Liver, LN	Chemotherapy and Hormone therapy

**Supplementary Table 3, Patient information pertaining to Figure 8E.**

Age, clinical characteristics and treatment received for patients with invasive ductal carcinoma (IDC) and from which CTC collected to assay PGC-1 $\alpha$  expression, CK8 and CD45 expression. IHC features: Immunohistochemical features of the primary tumor.

**Supplementary Table 4. Patient information related to Figure 8F**

	<b>Age (at blood collection)</b>	<b>Histopathological classification</b>	<b>IHC features</b>	<b>Stage</b>	<b>Metastasis</b>	<b>Treatment</b>
Patient 1	44	IDC	<i>Luminal B</i>	III	Lung	Chemo- and immunotherapy
Patient 2	44	IDC	<i>Luminal B</i>	NC	Lung, liver, bone, peritoneum	Chemo- and immunotherapy
Patient 3	54	IDC	<i>Triple negative</i>	I	Lung, hilar lymph node	Chemotherapy
Patient 4	53	IDC	<i>Her-2 overexpressing</i>	IV	Lung	Chemo- and immunotherapy
Patient 5	66	IDC	<i>Luminal B</i>	No data	Liver, lung, bone	Chemo- and immunotherapy
Patient 6	41	IDC	<i>Luminal B</i>	IV	Lung, CNS, bone	Chemo- and hormone therapy
Patient 7	44	IDC	<i>Luminal B</i>	I	Bone, lung, liver, lymph nodes	Chemo- and hormone therapy
Patient 8	29	IDC	<i>Luminal B</i>	IV	Liver, lung, bone	Chemotherapy
Patient 9	58	IDC	<i>Triple negative</i>	II	CNS, lung	Hormone therapy
Patient 10	44	IDC	<i>Luminal like [HR+ HER2(-)]</i>	II	Bone, lung, liver	Chemotherapy
Patient 11	31	IDC	<i>Her-2 overexpressing</i>	IV	Liver, lung	Immunotherapy and Targeted therapy
Patient 12	59	IDC	<i>Her-2 overexpressing</i>	IV	Lung	Chemo- and immunotherapy
Patient 13	58	IDC	<i>Luminal B</i>	IV	Bone, liver, lung, CNS	Chemo- and immunotherapy

**Supplementary Table 4, Patient information pertaining to Figure 8F.**

Age, clinical characteristics and treatment received for patients with invasive ductal carcinoma (IDC) and known metastasis to the lungs (and other listed sites) and from which detection of CTC was assayed and PGC-1 $\alpha$  expression determined. IHC features: Immunohistochemical features of the primary tumor.

**SupplementaryTable 5. Primer sequences**

Gene	Sequence
mo b-actin	F 5'-GGCTGTATTCCCCTCCATCG-3'
	R 5'-CCAGTTGGTAACAATGCCATGT-3'
mo PGC1a	F 5'-AGCCGTGACCACTGACAACGAG-3'
	R 5'-GCTCATGGTTCTGAGTCTAAG-3'
mo PGC1b	F 5'-GGACGCCAGTGACTTTGACT-3'
	R 5'-TTCATCCAGTTCTGGGAAGG-3'
mo NRF1	F 5'-CTGCTGTCTCTTTCCGATAGATC-3'
	R 5'-CGGAAACGGCCTCATCTCT-3'
mo UCP1	F 5'-GAGGTGTGGCAGTGTTCSTTG-3'
	R 5'-GGCTGCATTGTGACCTTCA-3'
mo ERRa	F 5'-AGGAAGCCCCGATGGA-3'
	R 5'-GAGAGGCCTGGGATGCTCTT-3'
Mo Elovl6	F 5'-AAGCAGTTC AACGAGAACGAA-3'
	R 5'-CGTACAGCGCAGAAAACAGG-3'
mo Cox5b	F 5'-GGAAGACCCTAATCTAGTCCCG-3'
	R 5'-CCACTATTCTTGTGTCTGAT-3'
mo Cox4i	F 5'-ATTGGCAAGAGGCCATTTCTAC-3'
	R 5'-CAACACTCCCATGTGCTCGAA-3'
mo ATPsynth (ATP5a1)	F 5'-GAGACTGGGCGTGTGTTAG-3'
	R 5'-CTCGACGCAATACCATCACCA-3'
mo CytC	F 5'-AAAGGGAGGCAAGCATAAGAC-3'
	R 5'-GAACAGACCGTGGAGATTTGG-3'
mo ACC (ACC265)	F 5'-ATGGGCGGAATGGTCTTTTC-3'
	R 5'-TGGGGACCTTGTCTTCATCAT-3'
mo FASN	F 5'-AGGTGGTGATAGCCGGTATGT-3'
	R 5'-TGGGTAATCCATAGAGCCAG-3'
mo CK8	F 5'-TCCATCAGGGTGACTCAGAAA-3'
	R 5'-CCAGCTTCAAGGGGCTCAA-3'
mo Twist	F 5'-CGGGAGTCCGAGTCTTA-3'
	R 5'-TGAATCTTGCTCAGTTGTC-3'
mo Snail	F 5'-TCCAACCCACTCGGATGTGAAGA-3'
	R 5'-TTGGTGCTTGTGAGCAAGGACAT-3'
mo aSMA	F 5'-GGCACCCTGAACCCTAAGG-3'
	R 5'-ACAATACCAGTTGTACGTCCAGA-3'
mo Ecad	F 5'-GAGCCTGAGTCTGACAGTCC-3'
	R 5'-TGTATTGCTGCTTGGCCTCA-3'
mo Slug	F 5'-CACATTGCAACCCACACATTGCCT-3'
	R 5'-TGTGCCCTCAGGTTTGATCTGTCT-3'
hu Actin	F 5'-CATGTACGTTGCTATCCAGGC-3'
	R 5'-CTCCTTAATGTACGCACGAT-3'
hu b-globin	F 5'-AGGAGAAGTCTGCCGTTACTG-3'
	R 5'-CTTCATCCAGTTCACCTTGC-3'
hu PGC1a	F 5'-GCTTTCTGGGTGGACTCAAC-3'
	R 5'-CTGCTAGCAAGTTTGCCTCA-3'
hu NRF1	F 5'-AGGAACCGGAGTGACCCAA-3'
	R 5'-TGCATGTGCTTCTATGGTAGC-3'
hu Cox5b	F 5'-ATGGCTTCAAGGTTACTTCGC-3'
	R 5'-CCCTTTGGGGCCAGTACATT-3'
hu Cox4i	F 5'-ACTACCCATGCCAGAAGAG-3'
	R 5'-TCATTGGAGCGACGGTTCATC-3'
hu ATPsynth	F 5'-TGCAAGGAATCCATGCCTC-3'
	R 5'-CGCCAGTTTCTTCAAGATCAA-3'
hu CytC	F 5'-CTTTGGGCGGAAGACAGGTC-3'
	R 5'-TTATTGGCGGCTGTGAAGAG-3'
hu ACC	F 5'-TGAGACTAGCAAACAATCTCGT-3'
	R 5'-AGAAAAGTAGAAGCTCCGATCCT-3'
hu FASN	F 5'-AAGGACCTGTCTAGGTTTGATGC-3'
	R 5'-TGGCTTATAGGTGACTTCCA-3'
hu Elovl6	F 5'-AGCAGTCAGTTTGTGACCAGG-3'
	R 5'-ATCTCCTAGTTCGGGTGCTTT-3'
hu Ecad	F 5'-CGAGAGCTACAGTTCACGG-3'
	R 5'-GGGTGTCGAGGGAAAAATAGG-3'
hu Twist	F 5'-CGGGAGTCCGAGTCTTA-3'
	R 5'-TGAATCTTGCTCAGTTGTC-3'
hu Snail	F 5'-GAGCCGGTGGCAGACTAG-3'
	R 5'-GACACATCGGTGAGACCAG-3'
hu aSMA	F 5'-GCTTTGAGCTTCCCTGAACA-3'
	R 5'-GGAGCTGCTTACAGGATTC-3'

**Supplementary Table 5, primer sequence.**

A list of primers used for quantitative PCR measurement of gene expression.

Figure S7A, percent <sup>13</sup>C label

	shscrbl			mean	SD	SE	shpgc-1a			mean	SD	SE
fructose-1,6-bi-P	98	98	96	97.242	1.152	0.665	98	96	96	96.446	0.995	0.574
fructose-6-bi-P	96	95	94	95.145	1.020	0.589	93	94	95	94.018	0.652	0.376
glucose-1-P	56	37	43	45.306	9.623	5.556	34	64	66	54.477	18.162	10.486
glucose-6-P	47	48	50	48.244	1.791	1.034	38	60	38	44.930	12.627	7.290
glyceraldehyd e-3-P	90	90	93	91.148	1.362	0.786	89	94	81	87.694	6.612	3.817
3-phosphoglyc erate	91	87	90	89.155	1.658	0.957	81	94	90	88.489	6.774	3.911
phosphoenol pyruvate	91	94	94	93.053	1.984	1.145	88	92	77	85.909	7.696	4.443
lactate	90	91	89	90.012	1.133	0.654	88	86	83	85.345	2.267	1.309
SBP	91	82	75	82.768	7.754	4.477	81	81	68	76.779	7.173	4.142
sedoheptulos e-7-P	79	76	83	79.458	3.640	2.102	81	82	83	82.197	1.253	0.724
O8P_O1P	38	56	57	50.172	10.491	6.057	44	40	48	44.025	4.088	2.360
xanthine	84	82	89	84.899	3.341	1.929	67	78	59	67.744	9.268	5.351
Glycine	82	76	66	74.446	7.764	4.483	78	40	36	51.007	23.052	13.309
Serine	3	5	3	3.695	0.957	0.552	3	1	1	1.790	1.145	0.661
sn-glycerol-3-P	74	82	82	79.531	4.431	2.558	81	77	81	79.779	2.300	1.328
UDP-D-glucose	92	88	93	90.812	2.788	1.610	93	94	84	90.219	5.408	3.122
UTP	42	40	52	44.629	6.640	3.834	41	47	47	44.924	3.768	2.176
glucosamine	91	94	93	92.339	1.474	0.851	79	81	93	84.515	7.792	4.499
Guanosine	66	56	66	62.932	5.586	3.225	56	74	64	64.618	9.017	5.206
N-acetyl-glucosamine-1-P	40	55	69	54.648	14.172	8.182	51	48	63	54.076	7.490	4.324
alanine	55	45	53	51.152	5.174	2.987	37	45	43	41.827	4.159	2.401
aspartate	1	0	0	0.556	0.361	0.208	0	0	0	0.332	0.184	0.106
D-gluconate	56	67	80	67.597	12.127	7.002	69	69	69	69.060	0.387	0.224
Glutamate	0	0	0	0.273	0.137	0.079	0	0	0	0.059	0.008	0.005
Urea	93	90	93	92.149	2.043	1.179	94	95	98	95.810	2.236	1.291
carnitine	98	98	96	97.481	1.158	0.669	98	98	97	97.589	0.804	0.464

Supplementary Table 6, statistics source data.

Source data indicating the percent <sup>13</sup>C label of listed metabolites in the indicated cell lines.